Greenhouse-Gas Induced Warming Amplification over the Arabian Peninsula with Implications for Ethiopian Rainfall

Kerry H. Cook, Edward K. Vizy, Yang Liu, Weiran Liu

Reference: Cook KH, Vizy EK, Liu Y, Liu W, 2021: Greenhouse-gas induced warming amplification over the Arabian Peninsula with implications for Ethiopian rainfall. *Climate Dynamics*, https://10.1007/s00382-021-05858-x.

ABSTRACT

Observed surface warming trends over the Arabian Peninsula are a factor of 1.4 – 2.1 greater than the tropical mean and a factor of 2.3 – 3.1 greater than the global mean. The primary reason for the amplified warming is the absence of latent cooling over the dry surface, not trends in net longwave heating or solar fluxes.

Well-validated regional model simulations with 30-km resolution are used to evaluate the implications of the amplified warming for the regional climate through the 21st century. Projected warming rates are similar to the observed ongoing warming, and low-level specific humidity increases by 50% by the end of the century. Precipitation increases occur only in summer in the southwest corner of the peninsula in association with enhanced orographic precipitation. Concurrent evaporation increases ameliorate and can even reverse increases in surface water availability associated with higher rainfall. A strengthening of the low-level negative meridional geopotential height gradient between the Arabian Peninsula and the Horn of Africa strengthens the zonal branch of the Somali jet, increasing westerly moisture transport into the Ethiopian Highlands and enhancing summer rainfall in northern Ethiopia by 20% at mid-century and by 35% by the end of the century. Confidence in the results is supported by the similarity of the projections with observed modes of variability and current trends.

1. Introduction

The Sahara Desert is warming at 3-4 times the rate of the globe – an amplified warming that is comparable to the high-latitude amplification associated with the ice albedo/temperature feedback (Cook and Vizy 2015, Vizy and Cook 2016). The purpose of this paper is to evaluate a similarly strong observed warming trend over the Arabian Peninsula and explore the implications for regional climate through the 21st century.

Background on the climate of the Arabian Peninsula and prior studies of observed and projected changes in the region is provided in the following section. Section 3 includes a description of the datasets used, analysis methods, and regional model simulations. Results are presented in section 4, and section 5 contains a summary and conclusions.

2. Background

The Arabian Peninsula is the largest peninsula in the world, covering approximately 3.2 million square kilometers and home to seven countries – Oman, United Arab Emirates, Qatar, Yemen, Bahrain, Kuwait, and Saudi Arabia. The climate is classified as arid desert and arid steppe, and elevation generally rises from the Persian Gulf coast in the east to the Red Sea coast in the west. The Arabian Peninsula is a major global-scale source of dust aerosols (Goudie 2014), especially during June through September (Kumar et al 2018, 2019).

The Arabian Peninsula is one of the warmest inhabited regions on the planet. Average boreal summer (June-July-August) temperatures exceed 32ºC over much of the peninsula, and 39ºC in the southeast. In June 2019, for example, Kuwait reported temperatures of 63ºC in direct sunlight and 52ºC in the shade. Interannual variations in surface temperature have been associated with various mode of natural variability, including ENSO and the North Atlantic Oscillation

(Chakraborty et al. 2006; Donat et al. 2014; Attada et al. 2016, 2018) and variations of the Indian monsoon (Attada et al. 2019).

Rainfall is sparse, with annual mean values below 0.5 mm/day nearly everywhere except in a small region with 2 mm/day in southwestern Saudi Arabia and western Yemen. While boreal summer is the dry season, about 40% of the precipitation is delivered in extreme events compared with 80% during the wetter winter season (Almazroui 2020).

This paper is motivated by the possibility that warming of the Arabian Peninsula induced by atmospheric greenhouse gas increases will be greater than the global mean. Recent observations and analysis indicate that the Sahara Desert is warming at 3-4 times the rate of the globe – an amplified warming that is comparable to the high-latitude amplification associated with the ice albedo/temperature feedback (Cook and Vizy 2015, Vizy and Cook 2017). The primary cause of the Saharan amplified warming is simply that the dryness of the surface prohibits the latent heat flux which is, in the rest of the tropics and subtropics, the primary mode of surface cooling. Changes in clouds do not play a discernible role. The warming amplification is somewhat stronger during the warm season due to an enhanced water vapor/temperature feedback. The amplified Saharan warming is associated with increased rainfall to the south and the recovery of Sahel rainfall in the 21st c., and both regional climate model (RCM) and CMIP5 coupled GCM simulations replicate the process in 21st c. projections (Vizy et al. 2013).

Several papers evaluate temperature trends over Saudi Arabia. Almazroui et al. (2012) find that surface temperatures averaged over Saudi Arabia increased at a rate of 0.72 K/decade in the dry season and 0.51 K/decade in the wet season over the 1979-2009 period. Reported trends in the diurnal temperature range are inconsistent in the literature. Almazroui et al. (2013) find that they are increasing, while AlSarmi and Washington (2011) report a significant decrease in association with strong warming at night.

Many studies that evaluate changes in extremes adopt standard measures developed by the Expert Team on Climate Change Detection and Indices (ETCCDI) and recommended by the World Meteorological Organization (WMO 2009). These measures have been applied to observed and modeled changes over the Arabian Peninsula, often averaged over a study region that includes northern Africa. In general, statistically-significant and spatially coherent changes in temperature but not precipitation are found (Zhang 2005). Donat et al. (2014) find that the warmest temperature of the year increased by 0.3 – 0.9 K/decade at various stations across the Arabian Peninsula over the 1981-2000 period. Nazril Islam et al. (2015) evaluated trends in Saudi Arabian temperature extremes for 1981-2010 at 27 stations and found that many stations exhibited statistically-significant positive trends in daily maximum temperature in boreal spring, summer, and fall.

Climate model projections indicate that these temperature trends will continue to increase, with stronger increases in summer. Lelieveld et al. (2016) examined output from 26 CMIP5 model projects under both the RCP4.5 and RCP8.5 emissions scenarios over a large region of the Middle East and Northern Africa that includes the Arabian Peninsula. The simulated multi-model mean trends were found to be consistent with observed trends, with temperature maxima projected to increase from 316 K (43ºC) to 319 K (46ºC) by mid-century and to 323 K (50ºC) by the century's end. This warming moves the large-scale regional average temperature from a "very strong heat stress" category into "extreme heat stress" (Abdel-Ghany et al. 2013), especially when exacerbated by expected increases in atmospheric moisture levels (Zhu et al 2019).

Donat et al. (2014) note that the regional mean rainfall over a large area of northern Africa and the Arabian Peninsula was anomalously high in the 1960s, so any evaluation of trends beginning then indicate significant drying. Trends calculated from the 1970s over the Arabian Peninsula show decreases in precipitation totals and the number of rainy days, but they are not statistically significant. Similarly, AlSarmi and Washington (2014) analyzed rainfall trends at 21 stations on the Arabian Peninsula and did not find a statistically-significant precipitation trend for 1980-2008. The only significant changes in rainfall measured was a decrease in the number of rainy days (rainfall > 10mm).

Ravi Kumar et al. (2019) reported a statistically significant increase in atmospheric dust loading over the Arabian Peninsula over the 2002-2012 decade. Rather than being associated with precipitation trends, which were not found, the aerosol trend was primarily associated with enhanced dust transport from the Sahara Desert, in particular through an intensification of a westerly jet that flows through the Tokar Gap in eastern Sudan.

These previous papers have thoroughly reported on trends in extremes using the full suite of ETCCDI indices in observations and the CMIP5 models. Here we do not focus on extreme events, but on changes in the regional climate as atmospheric greenhouse gas levels increase.

3. Methodology

a. Datasets

Multiple datasets are analyzed for the 1979-2018 period to improve confidence through comparison. For surface temperature, the following datasets are included:

- Climatic Research Unit CRUTEM4 dataset version 3.23 (CRU; Jones et al. 2012): A gridded dataset with 0.5º resolution that uses more than 4000 land-based weather stations to provide monthly land surface air temperature and precipitation estimates.

- Global Historical Climate Network CPC GHCN/CAMS merged land-ocean analysis (GHCN; Fan and van den Dool 2008): Monthly GHCN surface temperatures (version 3.2.2) are blended with Extended Reconstruction SSTs (ERSST version 3b) over the ocean to create this dataset. Station data are interpolated onto a 2.5° grid.
- Berkeley Earth Surface Temperatures (Rohde et al. 2013): This dataset merges approximately 37,000 land temperature records with HadSST3 ocean temperatures on a 1º grid.
- GISS Surface Temperature Analysis version 4 (GISS; Lenssen et al. 2019): Temperature observations from approximately 6300 land stations are combined with ocean temperatures from ERSSTv5 to produce monthly-mean values on a 2º grid globally.

Circulation and surface heat budget variables are examined in four atmospheric reanalyses, including the 1.5°-resolution ERA-Interim Reanalysis (ERAI; Dee et al. 2011), the 1.25°-resolution Japan Meteorological Agency's Japanese 55-Year Reanalysis (JRA-55; Kobayashi et al. 2015), the 0.5ºx 0.625º NASA Modern-Era Retrospective Analysis for Research and Applications (MERRA2; Gelaro et al., 2017), and the 0.25º ECMWF Re-Analysis 5 (ERA5; Copernicus Climate Change Service 2017).

Precipitation is evaluated in comparison with the 0.05º-resolution CHIRPS2 (Funk et al. 2015), the 0.25º TRMM 3B42 V7 (Huffman et al. 2007), and the 0.25º PERSIANN-CDR (Sorooshian et al. 2000) datasets.

b. Regional Model Simulations

The methodology used to generate climate change projections with a regional climate model was developed over many years, beginning with paleoclimate simulations, including over

Africa (Vizy and Cook 2005, 2007; Cook and Vizy 2006; Patricola and Cook 2007), that provide an opportunity to validate the simulated climate change against geological proxy data. The intent is to use regional climate modeling not as a downscaling tool, but as independently as possible from GCMs to avoid propagating GCM-error into the domain of the regional model and to provide a relatively independent simulation of climate change that can be compared with GCM simulations to evaluate confidence. The choice of a large domain maximizes this independence from GCMs, and the dependence on the lateral boundary conditions is minimal, especially in tropical applications.

The simulations analyzed here use a nested domain (Fig. 1) in the National Center for Atmospheric Research (NCAR) Weather Research and Forecasting model (WRF; Skamarock et al. 2005), fully described in Vizy el al. (2013). The outer domain, with 90-km resolution, covers all of Africa and the Arabian Peninsula, and also the Mediterranean, the Indian Ocean, and India (60ºW-100ºE; 50ºS-60ºN). The inner domain covers the Arabian Peninsula and all of Africa (30ºW-60ºE; 40ºS-40ºN) with 30-km resolution, chosen to provide a more accurate representation of topography, coastlines, and smaller-scale circulation features. The model time step is 3 min for the 90-km domain and 1 min for the 30-km domain.

In addition to providing higher resolution, regional modeling provides the ability to choose physical parameterizations that work well in the region of interest. Based on trial simulations, the following parameterizations are chosen for these integrations: Yonsei University planetary boundary layer (Hong et al. 2006); Monin–Obukhov surface layer; new Kain–Fritsch cumulus convection (Kain 2004); Purdue–Lin microphysics (Chen and Sun 2002); Rapid Radiative Transfer Model (RRTM) longwave radiation (Mlawer et al. 1997); Dudhia shortwave radiation (Dudhia 1989); unified Noah land surface model (Chen and Dudhia 2001).

The control simulation (CTL) runs from 1989 to 2008 after 292 simulated days for spin up, with the atmospheric CO_2 concentration set to 367 ppmv which is the 1989–2008 average observed at the Mauna Loa Observatory. SSTs and lateral boundary conditions for the 90-km domain are updated every 6 hours from NCEP2 (Kanamitsu et al. 2002). The inner domain is driven by the outer domain's solution of the model's governing equations using one-way nesting. The 20 years of the simulation are regarded as a 20-member ensemble of year-long integrations representing the climatology of 1989-2008.

Two additional 20-year simulations represent the climates of the mid- and late-21st c. (2041-2060 and 2081-2100, respectively), with atmospheric CO_2 levels set according to the IPCC's RCP8.5 emissions scenario at 564 ppmv and 850 ppmv, respectively. These are referred to as the M21 and L21 simulations. The 30-km simulation developed instabilities about halfway through the L21 integration because convective events became so strong that the equilibrium altitude for the rising parcels exceeded the 20-hPa top of the atmosphere set in the model. For this reason, the 30-km ensemble size for the late 21st c. has 9 members instead of 20. Comparisons with the 20-member ensemble at 90-km resolution provide assurance that the 9-member, high-resolution ensemble is an accurate representation of the simulated late 21st c. climate.

Lateral and initial boundary conditions and SSTs for the M21 simulation are modifications of the 6-hourly reanalysis values used in the CTL simulation. Anomalies derived from simulations with five CMIP5 coupled GCMs are used to adjust boundary conditions and SSTs. The RCP8.5-forced GCM simulations averaged over the 2041–2060 and 1986–2005 periods are assumed to represent the middle of the month, and linearly interpolated to generate anomalies every 6 h. These 6-hourly anomalies are averaged for the five GCMs, interpolated to the 90-km model grid, and added to the 6-hourly boundary conditions of the CTL simulation. The 1986–2005 period is used because it is the last 20 years available for the historical CMIP5 simulations. This use of multimodel mean anomalies minimizes the dependence of the projections on individual GCMs. The CMIP5 GCM outputs were examined individually to ensure that there are no obviously spurious values. The GCMs used are the NCAR Community Climate System Model version 4 (CCSM4), the Centre National de Recherches Meteorologiques Coupled Global Climate Model version 5 (CNRM-CM5), the Geophysical Fluid Dynamics Laboratory Climate Model version 3 (GFDL CM3), the Model for Interdisciplinary Research on Climate version 5 (MIROC5), and the Meteorological Research Institute Coupled GCM version 3 (MRI-CGCM3). A similar method is used for the L21 simulation, but for the 2080-2100 period. Output from the M21 and L21 simulations are treated as ensembles representing the mid- and late-21st c. climate.

Confidence in the model projections is assessed by several methods. The climate of the CTL simulation is compared with the observed climate as represented in multiple datasets as discussed above – a well-functioning present day climate adds to confidence in projections, although it does not guarantee accuracy. In addition, observed trends in surface temperature provide an opportunity for evaluating simulated trends. Differences between the M21 and CTL, and between the L21 and CTL, simulations are converted to trends assuming linearity to compare with observed warming rates. Further, the ensemble simulation design provides an opportunity to calculate the statistical significance of simulated changes. Understanding the physical processes of observed and simulated changes, and analogies to observed modes of variability, are also used to evaluate confidence.

c. Surface heat balance

The surface heat balance is used to understand observed surface temperature trends. Reliability in heat budget terms in reanalyses is not high because these terms are not assimilated and direct observations are sparse, so they are compared among the four reanalyses.

The heating rate of the surface is given by

$$C\frac{dT_S}{dt} = S_{ABS} + F_{BACK} - F_{UP} - H_S - H_L - D\,, \tag{1}$$

where T_S is surface temperature and C is the heat capacity of the surface. The surface is warmed by the absorption of solar radiation $\left(S_{ABS}\right)$ and longwave back radiation from atmospheric greenhouse gases $\left(F_{BACK}\right)$, and cooled by the emission of longwave (thermal) radiation from the surface, F_{UP}:

$$F_{UP} = \varepsilon\sigma {T_S}^4\,, \tag{2}$$

where ε is the longwave emissivity of the surface and σ is the Stefan-Boltzmann constant. Latent and sensible heat fluxes from the surface to the atmosphere, H_L and H_S, respectively, also cool the surface. D accounts for the redistribution of heat within the surface material. This term is expected to be small over land because diffusion is the only mechanism for moving heat within the surface. Over the oceans, D includes the roles of horizontal currents and upwelling/downwelling in moving heat into or out of a surface volume.

Heat balance terms are calculated for annual and seasonal means. On these time scales, $C\,{dT_S}/{dt}$ is negligible, as shown by the following estimate. C is given by

$$C = c\rho Z \tag{3}$$

where c is the specific heat capacity of the surface material, ρ is the density of the surface material, and Z is the depth to which the surface heating penetrates. Over land,

$$C \approx \left(840\ \ J/kg-K\right)\left(2.7x10^{3}kg/m^{3}\right)\left(0.02m\right) \approx 10^{4}\ \ J/m^{2}-K \tag{4}$$

and over an ocean surface

$$C \approx \left(4218\ \ J/kg-K\right)\left(10^{3}kg/m^{3}\right)\left(100m\right) \approx 10^{8}\ \ J/m^{2}-K \tag{5}$$

where an ocean mixed layer depth of Z~103 m is assumed. Using an estimate rate of warming of 1 K over 40 years,

$$C\frac{dT_S}{dt} \sim O\left(10^{4}J/m^{2}-K\right)O\left(10^{-10}K/s\right) \approx 10^{-6}\ \ W/m^{2} \tag{6}$$

for land and

$$C\frac{dT_S}{dt} \sim O\left(10^{8}J/m^{2}-K\right)O\left(10^{-10}K/s\right) \approx 10^{-2}\ \ W/m^{2} \tag{7}$$

for the ocean. Since the terms in the heat balance on the RHS of Eq. (1) are on the order of tens of W/m^2 (e.g., Cook et al. 2017), the time-dependent term on the LHS is negligible. Thus, the annual mean heat balance can be viewed as a series of equilibrium states and *D* can be calculated as a residual.

IV. Results

a. Observed surface temperature trends

Table 1 displays linear trends in annual-mean surface temperatures from four observational datasets and three reanalyses (section 3). Four averaging regions are used. The Arabian Peninsula region contains all land points from 15ºN to 25ºN and 40ºE to 55ºE. The tropics is defined as all points (both land and ocean) between 30ºS and 30ºN, while the tropical land average contains only land points between 30ºS and 30ºN. Global means are shown when available. Statistically significant values at the 90%, 95%, and 98% confidence levels are indicated.

All surface temperature trends in all datasets and all regions are positive, and nearly all are statistically significant at the 90% level or higher. Over the Arabian Peninsula, trends range from 0.28 K/decade in CRU to 0.58 K/decade in GHCN, and the reanalysis values fall within the range of the observations. The average rate of warming over the Arabian Peninsula is 0.39 K/decade.

Trends over the tropical mean, tropical land, and global mean are smaller than trends over the Arabian Peninsula. An amplification factor, defined as the Arabian Peninsula warming rate divided by the tropical or global warming rate, indicates that warming rates over the Arabian Peninsula are a factor of 1.4 – 2.1 greater than warming rates over the tropical land average, and a factor of 2.3 – 3.1 greater than global mean warming rates. These annual-mean amplification factors are similar to those of the Sahara Desert (Cook and Vizy 2015).

Warming trends are reported for each of the traditional seasons in Table 2. All trends are positive and most are statistically significant. The GHCN dataset consistently produces the largest values with lower statistical significance, similar to the annual mean values in Table 1. Over the Arabian Peninsula, warming trends are somewhat larger (18%) in the boreal spring and summer average (MAM and JJA) compared with the fall and winter mean (DJF and SON).

The components of the annual mean surface heat balance (section 3) are examined to understand the amplified warming of the Arabian Peninsula. Comparisons are made to the tropical mean rather than the global mean because the ice albedo-temperature feedback amplifies the high-latitude signal and this feedback does not operate over the Arabian Peninsula. Table 3 shows linear trends (W/m^2 per 40 years) in surface heat budget terms in the three reanalyses; standard deviations are shown in parentheses. Note that statistical significance is a useful guide, but a highly significant trend is not necessarily “correct” because of the concern that the surface heat budget terms and their variability are not accurate in reanalyses.

All three reanalyses produce negative, or cooling, trends in the solar radiation absorbed over both the tropical and Arabian Peninsula averaging regions, but statistical significance above the 90% level does not emerge. In each reanalysis the solar radiation cooling trend is a few W/(m^2-40 yr) smaller over the Arabian Peninsula than in the tropical mean, so this difference could be associated with the amplified heating over the Arabian Peninsula. The association may be causative or responsive.

In both ERAI and JRA55, increases in the longwave back radiation are highly significant in both the tropical and Arabian Peninsula averages; MERRA2 produces similarly large but less significant trends. Increasing levels of atmospheric greenhouse gases have increased the longwave back radiation by roughly 1 W/m^2 in the last 40 years, with uniform distribution over the globe since CO_2 is well-mixed in the atmosphere. The estimates of trends in the longwave back radiation shown in Table 3 are greater than 1 W/m^2-40 yr so they cannot be explained by increases in atmospheric greenhouse gases alone. Also, they are larger over the Arabian Peninsula than in the tropical mean, and this would not be expected as a direct response to anthropogenic CO_2 since it is well mixed in the atmosphere. Rather, as discussed below, these upward trends in the longwave back radiation are related to trends in the surface emission of longwave radiation.

Upward longwave fluxes also exhibit positive trends, with larger values over the Arabian Peninsula, reflecting the differences in the surface temperature trends in the tropical and Arabian Peninsula means. Strong coupling between the longwave back radiation and the upward longwave radiative flux from the surface explains the upward trends in the back radiation, including its amplification over the Arabian Peninsula. Trends in the net upward longwave flux ($F_{UP} - F_{BACK}$) and in the net radiative heating of the surface ($S_{ABS} + F_{BACK} - F_{UP}$) are small and generally insignificant (Table 3). The longwave component of the heat budget cannot explain the trend.

Trends in the tropical-mean sensible heat flux are small (<0.5 W/m^2) and statistically insignificant in the reanalyses, and somewhat larger (1-2 W/m^2-40 yr) over the Arabian Peninsula. The sensible heat flux is responsive to surface temperatures, so these differences are consistent with the amplified warming of the Arabian Peninsula but not explanatory.

Large trends occur in the tropical-mean latent heat flux and the redistribution term. In the tropical mean, which includes extensive ocean areas, surface warming trends (Tables 1 and 2) are accompanied by large positive latent heat flux trends (5-9 W/m^2-40 yr), i.e., increases in evaporative cooling. This cooling mechanism is partially balanced by a warming mechanism; the negative values of the redistribution term indicate that ocean currents are contributing to a warming of the tropical ocean surface that counteracts, and even overwhelms, the evaporative cooling trend. A more detailed discussion of these compensating mechanisms over the tropical oceans is outside the scope of this paper. See, for example, Drenkard and Karnauskas (2014), Yang et al. (2014), and Cook and Vizy (2019a).

The large positive trends in the latent heat flux in the tropical mean are not seen over the Arabian Peninsula. Here, trends are small and negative. Similarly, the large negative trends in the redistribution term that occur in the tropical mean do not occur over the Arabian Peninsula, as expected for any land point.

We conclude that the reason for the amplified warming over the Arabian Peninsula compared with the tropical mean is simply that an evaporative response to greenhouse gas forcing is not possible over the dry surface. This is the same result as over the Sahara Desert (Cook and Vizy 2015; Vizy and Cook 2017). Similar to that analysis, the roles of clouds and changes in atmospheric water vapor are not the primary cause of the amplified surface temperature response to greenhouse gas forcing, and the tight coupling between the upward and downward longwave fluxes obscures the direct effects of the added back radiation from increasing greenhouse gases.

b. Model evaluation

Before examining projected trends, we evaluate the realism of the CTL ensemble simulation. Surface temperature seasonal averages over the Arabian Peninsula from the CTL ensemble mean are displayed in Figures 2a-d, with comparable values from the ERAI reanalysis in Figures 2e-h. Surface temperature climatologies are similar to ERAI in the other reanalyses. The simulation captures the distributions, magnitudes, and seasonality of surface temperature over the Arabian Peninsula with good accuracy, exceeding the realism of the CMIP5 multi-model mean as presented by Almazroui et al. (2020). A surface temperature gradient is oriented from the northwest to the southeast in DJF, MAM, and SON. The boreal fall surface temperature distribution (Figs. 2d and h) is very similar to the spring distribution (Figs. 2b and f). Surface temperatures are more uniform in boreal summer (Figs. 2c and g), with temperatures a few degrees higher in the eastern part of the peninsula.

The low-level circulation, represented by 925-hPa geopotential heights (shaded) and winds (vectors), and specific humidity (contours) in the CTL simulation for the traditional seasons is shown in Figures 3a-d. The same fields from the ERAI reanalysis are shown in Figures 3e-h. In DJF, geopotential height gradients are small across the peninsula, with easterly flow across the southern half. Patterns are similar in MAM and SON. In boreal summer, however, low geopotential heights cover the Arabian Peninsula and the flow is northerly. The low pressures are a westward extension of the Indian monsoon trough.

Figure 4a shows line plots of the daily 850-hPa geopotential height (red lines) and surface temperature (green lines) along with 500-hPa geopotential height (blue lines) averaged over the Arabian Peninsula (15ºN – 30ºN; 35ºE to 55ºE) in the CTL ensemble mean; Fig. 4b shows the same fields from the ERAI climatology. The 850-hPa level is chosen for the area average because it largely clears the regional topography. The increase in 500-hPa geopotential heights from January through May reflects the seasonal formation of the Arabian high, which is strongest in both the model simulation and reanalysis at this level. The Arabian high forms over the southern portion of the peninsula in May, and remains in place through September. As seen in the June, July, August, and September (JJAS) mean shown in Figures 5a and b, the presence of the Arabian high maintains anticyclonic circulation over the Arabian Peninsula during these warm months. The thermal low/Arabian high structure is strengthened during years in which the Indian summer monsoon is strong (Attada et al. 2019). Consistent with Fig. 4, geopotential height anomalies associated with the simulated Arabian high are stronger in the model than in the ERAI reanalysis. (This is also the case when the simulation is compared with the other reanalyses.) During the rest of the year, the upper-level flow over the Arabian Peninsula is westerly in association with zonally-uniform, negative geopotential height gradients (e.g., Figs. 5c and d).

The simulated precipitation climatology from the CTL ensemble mean is compared with the CHIRPS climatology averaged over the same years (1989-2008). In Figure 6, a larger domain is adopted to show rainfall in the regions surrounding the Arabian Peninsula. While the model tends to over-produce rainfall over the Horn of African compared with CHIRPS, it produces rainfall rates over the Arabian Peninsula that are lower than in the observations. The differences, however, are relatively small, and the geographic distribution is realistic in the simulation.

c. Projected trends

Table 4 shows seasonal and annual surface temperature differences averaged over the Arabian Peninsula region simulated in the M21 and L21 ensemble simulations; differences are relative to the CTL simulation. Warming rates in units of K/decade are calculated to facilitate the comparison with observed rates in Tables 1 and 2.

In both the annual and seasonal means, all surface temperature differences in both the M21 and L21 simulations exceed the 98th percentile in statistical significance. Even monthly mean values (not shown) are significant at the 98th percentile with the exception of February and November. During these months the standard deviation of temperatures is greater and the temperature differences are significant at the 95th percentile.

Rates of surface temperature change are calculated by dividing the differences between the M21 and L20 temperatures by 5.2 decades, representing the 52-year time difference between the midpoints of each 20-member ensemble (1998 and 2050). For the L21 simulation, the time difference is 102 years. In both the M21 and L21 simulations, the warming rate is somewhat greater in the boreal summer and fall than in the winter and spring. There is no suggestion that the warming rate accelerates or decelerates in the second half of the century.

The annual mean rates of surface temperature change for the Arabian Peninsula in the model (about 0.5 K/decade; Table 4) are a little larger than the observed average (about 0.4 K/decade; Table 1), but the modeled rates fall with the range of the observations by being less than the GHCN value. The same is true for the DJF, JJA, and SON seasonal means. The simulated MAM warming (0.46 K/decade; Table 4) is close to the observed mean (0.44 K/decade; Table 2).

The regionality of the projected surface warming across the Arabian Peninsula as a function of season for the M21 simulation is presented in Figures 7a-d, and for the L21 simulation in Figs. 7d-h. In DJF and MAM, the strongest warming is in the southern half of the peninsula where the warmest current temperatures occur (compare with Fig. 2). Temperature differences are up to 3 K in the mid-21st c. simulation, and 5 K in the late-21st c. simulation. Temperature differences are much larger in JJA – exceeding 3 K in the M21 simulation and about double in the L21 simulation - but still largest in the southern half of the Arabian Peninsula. Large temperature differences are more widespread in boreal fall and exceed 3 K (6 K) over a large fraction of the peninsula in the M21 (L21) simulation. There is not a strong diurnal cycle in the simulated temperature differences.

Changes in the low-level circulation accompany the simulated warming. Figures 8a-d show seasonal differences in 850-hPa geopotential heights and winds for the M21 simulation; numbers in the upper right corner of each panel indicate differences in geopotential heights (gpm) and percent differences in specific humidity over the Arabian Peninsula averaging region (15-25N; 40-55E). Figures 8e-h are the L21 – CTL differences. In each case, geopotential height anomalies are positive everywhere because the global atmosphere expands vertically as it warms.

In DJF and MAM, easterly flow anomalies develop over the northern Arabian Peninsula by the mid-21st c. (Fig. 8a and b) in association with positive geopotential height anomalies to the northwest. Comparison with the full fields in Fig. 3 indicates that this response amounts to a reduction in the weak westerly flow that crosses the northern Arabian Peninsula in boreal winter. In the L21 simulation, anomalous northeasterly flow associated with a deepening of the anomalous high over the southeast Mediterranean replaces the weak anticyclonic circulation of the late 20th c. in DJF (Fig. 8e) but this pattern does not persist into the spring (Fig. 8f). Overall, the weak positive geopotential height gradient that characterizes the boreal fall and spring in the 20th c. climate (Fig. 3), with small increases in geopotential height from the northwest to the southeast across the Arabian Peninsula, becomes even weaker in the future simulations.

The JJA climatology of the 20th c. (Figs. 3c and g) features a low-level geopotential height gradient that is opposite to that of the winter and spring, with decreasing geopotential height from the northwest to the southeast across the Arabian Peninsula. As seen in Figs. 8c and g, this gradient is also weakened in the future simulations. The resulting flow anomalies are predominantly southerly, weakening the northerly flow of the late 20th c. climatology (Fig. 3).

In contrast to the other seasons, there is some intensification of the late 20th c. climatological low-level flow in boreal fall with strengthened northeasterlies (Figs. 3d and h; Figs 8d and h). The anomalies are associated with lowered geopotential heights over the southern peninsula as the winter anomalies (Figs. 8a and e) reestablish.

Low-level specific humidity increases in each season for both the M21 and L21 simulations over the dry Arabian Peninsula. The increases are fairly uniform, and indicated as an average in each panel of Fig.8. The primary source of this excess moisture is not enhanced evaporation from the dry Arabian Peninsula since there are no widespread increases in water availability at the surface (shown below). Nonetheless, the changes in specific humidity roughly follow the Clausius-Clapeyron relation that predicts a 6-7% increase in evaporation and atmospheric vapor pressure with each 1 K warming, assuming constant relative humidity. The seasonal-mean specific humidity increases shown in Fig. 8 range between 5.8 %/K and 8.7 %/K, with larger values occurring primarily in summer and fall.

Figures 9a and b show 500-hPa geopotential heights from CTL and L21 in July, when the Arabian high is fully formed (Fig. 4). Differences between the CTL and M21 simulations are smaller but similar in structure, so we show only the L21 differences for brevity. Note that the structure of the Arabian high is similar in the future simulation, but the geopotential heights in L21 are 100 hPa greater in association with an overall expansion of the warmed atmosphere. (At this level, geopotential heights in the M21 simulation are about 50 hPa greater than in the CTL simulation.) Because of these large-scale changes, it is difficult to quantify changes in the Arabian high using geopotential height. Therefore, we also examine the relative vorticity (Figs. 9c and d). Note that, unlike the geopotential height Figs. 9a and d, the contour levels are the same in Figs. 9c and d. Quantified by the relative vorticity, the Arabian high is not changed in the future simulations. The result is the same at adjacent vertical levels and during the other months during which the Arabian high forms (May through September).

In general, the extremely low precipitation rates that characterize the Arabian Peninsula remain low in the future simulations. A noteworthy exception occurs during the warm season in the southwest corner of the Arabian Peninsula, where annually-averaged rainfall rates exceed 1 mm/day in the current (Fig. 6). In May, precipitation in this region increases by less than 0.5 mm/day by the end of the century (0.2 mm/day at mid-century). Rainfall increases become more widespread by July and reach 0.8 mm/day in the L21 simulation (Fig. 10a). In August, as shown in Fig. 10b for the L21-CTL difference, these differences amount to more than a doubling of rainfall. September anomalies are small (Fig. 10c), and negligible for other months.

Evaporation increases driven by warming surface temperatures accompany the southwestern precipitation increases, as shown in Figs. 10d-f for July through September. In July and August, the positive evaporation anomalies are smaller than the precipitation anomalies. In these months, water availability (measure by “precipitation minus evaporation’) at the surface is increased in the southwest region, especially in August (Figs. 10g and h). In September, precipitation increases are exceeded by evaporation increases. The net result is surface drying, despite the precipitation increase (Fig. 10i).

To understand these simulated precipitation increases more fully, Figure 11a shows a close-up of the circulation centered on the southwestern peninsula from the CTL simulation at 800 hPa for August. Zonal geopotential height gradients are located to the west of the Arabian Peninsula, while geopotential height gradients over the Arabian Peninsula and to the south are primarily meridional. A well-formed geostrophic flow follows this pattern, with northerly flow over the Red Sea and westerly flow – part of the Somali jet (Findlater 1969) – to the south of the Arabian Peninsula over the Gulf of Aden. This large scale pattern is similar at 925 hPa (Fig. 11b), but at this level the flow over the Red Sea is northwesterly south of 19ºN.

The monsoon trough extends westward over the Arabian Peninsula between 14ºN and 18ºN. Rainfall in the southwest is supported when moisture transport from the northeast at 800 hPa associated with the trough impinges on the topography. At this level (Fig. 11a), moisture transport to the west of the topography largely parallels the coastal mountains. At 925 hPa (Fig. 11b), moisture transport to the west of the coastal topography has more interaction with the topography; associated orographic rainfall occurs south of 17ºN. The influence of the Tokar Gap (18ºN and 38ºE) is apparent at both the 925 hPa and 800 hPa levels.

Differences in the 800-hPa and 925-hPa geopotential heights and moisture transport vectors between the CTL and L21 simulations are shown in Figs. 11c and d, respectively. At 800 hPa, the strengthening and northwestward extension of the monsoon trough over the Arabian Peninsula enhances northeasterly moisture transport onto the coastal topography north of 16ºN. Over the Red Sea, the anomalous geopotential height gradient is meridional so the anomalous flow attains a westerly component that also supports the orographic precipitation anomaly. At 925 hPa, the meridional geopotential height gradient over the Red Sea is weakened in the L21 simulation. The anomalous moisture transport is westerly, which further enhances the orographic rainfall in the southwestern Arabian Peninsula (Fig. 10b). Again, anomalies for the M21-CTL difference are similar to the L21-CTL differences, but about half the magnitude.

Figure 11 shows that the amplified warming of the Arabian Peninsula strengthens the negative meridional geopotential height gradient between the Arabian Peninsula and the Horn of Africa, and that these enhanced gradients are associated with a strengthening of the zonal branch of the Somali Jet. The anomaly fields are very similar to those shown by Attada et al. (2019) for differences between strong and weak Indian summer monsoon composites (e.g., Fig. 5b in Attada et al. 2019); a strong Indian monsoon is also associated with a strong Somali jet. Figure 12 provides a larger-scale perspective in showing 850 hPa geopotential heights (shaded), moisture transport vectors, and precipitation (contours) from the 90-km resolution outer domain (Fig. 1). The direct connection between the zonal moisture transport by the Somali jet over the Gulf of Aden and the westerly transport of moisture onto the west coast of India is evident in the full fields (Fig. 12a), and their enhancement in the L21 simulation is evident in the difference field (Fig. 12b).

Figure 11 also indicates that elevated greenhouse gases increase southwesterly moisture transport over Sudan and northwestern Ethiopia. This not only increases transport through the Tokar Gap, as noted above, but also increases interactions with the topography of the Ethiopian highlands, especially in the 825 – 700 hPa layer (Fig. 11c). Summer is the rainy season for northern Ethiopia - a single wet season with strong orographic rainfall. The simulation captures this seasonality but, as shown in Fig. 13 in a comparison with the TRMM climatology for 1998-2019 (PERSIAN and CHIRPS are similar), simulated rainfall rates are too large (see also Fig. 6). Summer rainfall rates over northern Ethiopia (36ºE-42ºE; 8ºN-15ºN) increase by about 20% at mid-century, and by about 35% by the end of the century in the simulations. In addition, the end of the rainy season is delayed by approximately 2 weeks by the end of the century (Fig. 13).

Not all of the differences shown in Fig. 12 are attributable to the amplified warming of the Arabian Peninsula. However, we can associate the enhanced rainfall of northern Ethiopia in the L21 simulation (Fig. 12b) with the strengthening of the zonal branch of the Somali jet and, thereby, Arabian Peninsula warming by analogy with an observed mode of natural variability in the current climate. This mode is characterized by a positive correlation between monsoon rainfall in India and summer rainfall in Ethiopia through the strength of the zonal branch of the Somali Jet (Camberlin 1995 and 1997, Vizy and Cook 2003). Note that the precipitation response over Ethiopia in summer is not a direct response to the increases in greenhouse gases and SST differences applied in the L21 (and M21) simulations, but a secondary response to amplified warming of the Arabian Peninsula.

As an additional method for evaluating confidence in the projections of increased Ethiopian rainfall in summer, we examine observed trends in the low-level circulation and compare them with the simulated differences for the mid- and late21st c. [Because they are notoriously noisy, examining precipitation fields directly to evaluate their change requires extensive analysis that is beyond the scope of this paper, although we note that there are indications that summer rainfall in northern Ethiopia is experiencing a positive trend (e.g., Fig. 4b in Cook and Vizy 2019b).] Here we evaluate circulation trends by plotting decadal differences in the 850-hPa geopotential heights and winds (Fig. 14). Since caution is indicated when using reanalyses for analyzing trends, we present results from 4 reanalyses. In three of the four reanalyses, namely, ERAI (Fig. 14a), ERA5 (Fig. 14b), and MERRA2 (Fig 14c), the thermal low over the southern Arabian Peninsula is stronger in the more recent climatology, accompanied by increases in the meridional geopotential height gradient over the northern Arabian Sea and a stronger zonal branch of the Somali jet. In addition, all three reanalyses indicate an increase in the westerly flow impinging on the Ethiopian highlands, similar to the model projections. A strengthening of the thermal low over the Arabian Peninsula and enhanced westerly flow west of the Ethiopian Highlands north of 10ºN also occurs in the JRA-55 reanalysis, but a strengthening of the zonal branch of the Somali jet over the northern Arabian Sea is not clearly indicated, and the anomalous flow in some regions seems inconsistent with the anomalous geopotential height field. This could occur because the sea surface temperature prescription in the JRA-55 reanalysis uses only ground-based measurements with no satellite-derived values included – a potential concern in this region with sparse in situ observations.

V. Summary and Conclusions

Motivated by the observed amplification of the greenhouse gas-induced warming of the Sahara Desert, trends in observed surface temperatures and reanalyzed surface heat balance components are examined over the Arabian Peninsula. High resolution (30 km) model simulations are used to evaluate the implications for the regional climate through the 21st century.

Surface temperature trends in multiple observational and reanalysis datasets averaged over the Arabian Peninsula are compared with global and tropical mean trends. Surface warming trends over the Arabian Peninsula are a factor of 1.4 – 2.1 greater than over all tropical land points, and a factor of 2.3 – 3.1 greater than global mean warming rates. Warming rates over the Arabian Peninsula are 18% greater in the boreal spring and summer average compared with the fall and winter. An examination of reanalyzed surface heat balance trends shows that the primary reason for the amplified warming signal over the Arabian Peninsula is the absence of a latent cooling anomaly over the dry surface. Trends in the net longwave heat flux at the surface are insignificant because the upward and downward fluxes are tightly coupled, and there are no explanatory trends in the solar radiative or sensible heating terms.

Regional model simulations representing the 1989-2008 climatology with twenty ensemble members at 30-km resolution are evaluated through comparison with reanalyses. The model climatology over the Arabian Peninsula is quite accurate, and captures the seasonal evolution of temperature, precipitation, and circulation over the Arabian Peninsula well.

Two additional ensemble simulations represent the mid- and late-21st c. under atmospheric CO_2 increases set according to the IPCC's RCP8.5 emissions scenario. As a means of evaluating the realism of these projections, Arabian Peninsula surface temperature anomalies in the future simulations are translated into rates of change per decade for comparison with the observed warming. For the annual mean, simulated rates of surface temperature change over the Arabian Peninsula are about 0.5 K/decade throughout the 21st c., just a little larger than the observed average of about 0.4 K/decade but within the range of observed values. Simulated temperature differences exhibit higher seasonality than the observations, with warming rates about 0.1 K/decade larger in the warmer seasons of summer and fall than in winter and spring.

In boreal winter, spring, and fall, the low-level circulation weakens with increasing greenhouse gas levels since the geopotential height anomalies act to weaken gradients. In the fall, however, the climatological northeasterly flow is strengthened in association with lower geopotential height anomalies over the southern peninsula.

Percentage changes in low-level specific humidity through the 21st c. are large and positive. For example, summer 925-hPa specific humidity increases by 24% at mid-century, and by 49% at the end of the century in the simulations, roughly consistent with the Clausius-Clapeyron scaling. These increases have profound implications for thermal stresses on humans, livestock, and wild animals as well as agricultural and natural vegetation (Abdel-Ghany et al. 2013) and, combined with temperature increases, will bring the region past a threshold level of habitability before the end of the century (Pal and Eltahir 2016).

While the low precipitation rates of the Arabian Peninsula generally persist in the future simulations, rainfall increases in the southwest during the warm season. A small, localized precipitation enhancement in May expands until August, with increases of nearly 1 mm/day at the end of the century in the simulations - a doubling of the present-day rainfall. These precipitation increases are accompanied by increases in evaporation associated with surface warming, so changes in surface water availability are more limited. In July and August, the positive evaporation anomalies are smaller than the precipitation anomalies so water availability at the surface is increased in the southwest region. In September, precipitation increases are exceeded by evaporation increases and the net result is surface drying.

Confidence in the projections is evaluated by examining the associated physical processes and comparing them with observed trends and known modes of variability. Precipitation increases in the southwest are related to changes in the low-level flow and associated moisture transport. In the simulations of the mid- and late-21st c., amplified warming of the Arabian Peninsula in the warm season - which occurs at a rate that is similar to the observed warming – causes an extension of the thermal low across the Arabian Peninsula between 14ºN and 18ºN. The associated strengthening of the northeasterly flow in the 750-850 hPa layer transports more moisture to interact with the coastal topography north of 16ºN, in partial support of the precipitation enhancement. West of the topography, at lower levels over the Red Sea, the northerly flow of the present day is perturbed by a westerly anomaly. The resulting westerly moisture transport anomaly further enhances the orographic rainfall in the southwestern Arabian Peninsula during summer.

While the precipitation response on the Arabian Peninsula to increasing atmospheric greenhouse gases is relatively modest, the analysis shows that summer rainfall over northern Ethiopia is strongly influenced. The amplified warming of the Arabian Peninsula strengthens the negative meridional geopotential height gradient between the Arabian Peninsula and the Horn of Africa, resulting in a strengthening of the zonal branch of the Somali Jet. Consistent with a known mode of variability that connects monsoon rainfall in India with summer rainfall in northern Ethiopia through the strength of the zonal branch of the Somali Jet, westerly moisture transport into the Ethiopian Highlands is associated with a 20% increase in rainfall at mid-century and a 35% increase by the end of the century in the simulations. These anomalies are not a direct response to the anomalous CO_2 radiative forcing and SST differences applied in the simulations; they are secondary response to the amplified warming of the Arabian Peninsula. Very similar trends in the low-level circulation occur in atmospheric reanalyses since 1979.

While temperatures are increasing at virtually every location on the earth, health concerns related to these increases may be especially imperative in the warmest inhabited regions. Many of these warm regions are located in or near the subtropical deserts where anthropogenically-induced temperature trends are, in general, amplified and there is concern that temperatures may reach the limits of human habitability by the end of the twenty-first century. Changes in precipitation are also crucial since much of Ethiopian agriculture is rainfed.In addition, water resources across the Arabian Peninsula depend on a network of dams and irrigation that draws on fossil water stored in aquifers during the wetter climates of the Pleistocene glacial periods that is not being replenished in the current climate. Ongoing greenhouse gas-induced warming increases evaporation rates and can accelerate the use of this resource.

Next steps in advancing our capability to produce reliable projections over the Arabian Peninsula is running convective permitting simulations with, for example, 3 km resolution to better capture small-scale processes and storm development.

Acknowledgements: Support from NSF Award #1701520 is gratefully acknowledged. The Texas Advanced Computing Center (TACC) at The University of Texas at Austin provided the HPC and database resources that were critical to the research results reported in this paper.

References

Abdel-Ghany AM, Al-Helal IM, Shady MR (2013) Human thermal comfort and heat stress in an outdoor urban arid environment: a case study. Advances in Meteorology: 2013 Art. No. 693541. https://doi.org/10.1155/2013/693541

Almazroui M, Islam MN, Jones PD, Athar H, Rahman MA (2012). Recent climate change in the Arabian Peninsula: seasonal rainfall and temperature climatology of Saudi Arabia for 1979–2009. Atmospheric Research, 111, 29-45.

Almazroui M, Islam MN, Dambul R, Jones PD (2013) Trends of temperature extremes in Saudi Arabia. Int. J. Climatol. 34: 808–826, https://doi 10.1002/joc.3722

Almazroui M, Saeed S (2020) Contribution of extreme daily precipitation to total rainfall over the Arabian Peninsula. Atmos. Research. https://doi.org/10.1016/j.atmosres.2019.104672

AlSarmi S, Washington R (2011) Recent observed climate change over the Arabian Peninsula. J. Geophys. Res. 116: D11109. https://doi.org/10.1029/2010JD015459

AlSarmi S,Washington R (2014) Changes in climate extremes in the Arabian Peninsula: analysis of daily data. Int. J. Climatol. 34: 1329–1345, https://doi.org/10.1002/joc.3772.

Attada R, Dasari HP, Chowdary JS, Yadav RK, Knio O, Hoteit I (2016) Surface air temperature variability over the Arabian Peninsula and its links to circulation patterns. Int. J. Climatology, 39: 445-464. https://doi.org/10.1002/joc.5821

Attada R, Kumar RK, Yadav RK, Dasari H P, Knio O, Hoteit I. (2018) Prominent modes of summer surface air temperature variability and associated circulation anomalies over the Arabian Peninsula. Atmos. Sci. Lett., 19: e860, https://doi.org/10. 1002/asl.860.

Attada R, Dasari HP, Parekh A, Chowdary JS, Langodan S, Knio O, Hoteit I (2019) The role of the Indian summer monsoon variability on Arabian Peninsula summer climate. Climate Dynamics 52: 3389-3404. https://doi.org/10.1007/s00382-018-4333-x

Chakraborty A, Behera SK, Mujumdar M., Ohba R., Yamagata T. (2006). Diagnosis of tropospheric moisture over Saudi Arabia and influences of IOD and ENSO. Mon. Weather. Rev. 134: 598–617, https ://doi.org/10.1175/MWR3085.1.

Donat MG, Peterson TC, Brunet M, King AD and co-authors (2014) Changes in extreme temperature and precipitation in the Arab region: Long-term trends and variability related to ENSO and NOA. Int. J. Climatology 34: 581-592. https://doi.org/10.1002/joc.3707

Drenkard, E.J., and K.B. Karnauskas, 2014: Strengthening of the Pacific equatorial undercurrent in the SODA reanalysis: Mechanisms, ocean dynamics, and implications; J/ Climate, 27, 2405-2416.

Camberlin P (1995) June-September rainfall in northeastern Africa and atmospheric signals over the tropics: A zonal perspective. Int. J. Climatology: 15, 773-783.

Camberlin P (1997) Rainfall anomalies in the source region of the Nile and their connection with the Indian summer monsoon. J. Climatology: 10, 1380-1392.

Chen F, Dudhia J (2001) Coupling an advanced land surface–hydrology model with the Penn State–NCAR MM5 modeling system. Part I: Model description and implementation. Mon. Wea. Rev., 129: 569–585.

Chen, S-H, Sun Y-W (2002) A one-dimensional time dependent cloud model. J. Meteor. Soc. Japan, 80: 99–118.

Copernicus Climate Change Service (2017) ERA5: Fifth generation of ECMWF atmospheric reanalyses of the global climate . Copernicus Climate Change Service Climate Data Store (CDS). https://cds.climate.copernicus.eu/cdsapp#!/home

Cook KH, Vizy EK (2006) South American climate during the Last Glacial Maximum: Delayed onset of the South American monsoon. J Geophys Res Atmos 111 (D2): 2110. https://doi.org/10.1029/2005JD005980

Cook KH, Vizy EK, Sun X (2017) Multidecadal-scale adjustment of the ocean mixed layer heat budget in the tropics: Examining ocean reanalyses. Climate Dynamics: 50, 1513-1532. doi.org/10.1007/s00382-017-3703-0

Cook KH, Vizy EK (2015) Detection and analysis of an amplified warming of the Sahara Desert. J Clim 28: 6560-6580. https://doi.org/10.1175/JCLI-D-14-00230.1

Cook, KH, Vizy EK (2019a) Examining multidecadal trends in the surface heat balance over the tropical and subtropical oceans in atmospheric reanalyses. *Int. J. Climatol*: 40, 2253-2269. https://rmets.onlinelibrary.wiley.com/doi/abs/10.1002/joc.6330

Cook, KH, Vizy EK (2019b) Contemporary climate change of the African monsoon systems. Current Climate Change Reports, 5, 145-159.https://doi.org/10.1007/s40641-019-00130-1

Dee, DP, Uppala SM, Simmon AJ, and co-authors(2011) The ERA-Interim reanalysis: Configuration and performance of the data assimilation system. Q. J. Roy. Meteorol. Soc., 137, 553-597.

Drenkard EJ, Karnauskas KB (2014) Strengthening of the Pacific equatorial undercurrent in the SODA reanalysis: Mechanisms, ocean dynamics, and implications. J. Climate: 27, 2405-2416.

Dudhia J (1989) Numerical study of convection observed during the winter monsoon experiment using a mesoscale two-dimensional model. J Atmospheric Sci: 46, 3077-3107.

Fan Y, Van den Dool H (2008) A global monthly land surface air temperature analysis for 1948–present. J. Geophysical Research – Atmospheres: 113(D1). https://doi.org/10.1029/ 2007JD008470

Findlater J (1969) A major low-level air current near the Indian Ocean during the northern summer. Q. J. R. Meteorol. Soc: 95, 362– 380.

Funk C, Peterson P, Landsfeld M, Pedreros D, Verdin J, Shukla S, Husak G, Rowland J, Harrison L, Hoell A, Michaelsen J (2015) The climate hazards infrared precipitation with stations – a new environmental record for monitoring extremes. Scientific Data: 2, 150066. https://doi.org/10.1038/sdata.2015.66

Gelaro R, McCarty W, Suarez M, Todling R, Molinaro A, and co-authors (2017) The Modern-Era Retrospective Analysis for Research and Applications, version 2 (MERRA-2). J. Climate: 30, 5419-5454. https://doi.org/10.1175/JCLI-D-16-0758.1

Goudie AS (2014) Desert dust and human health disorders. Environment International 63: 101–113. https://doi.org/10.1016/j.envint.2013.10.011

Hong S-Y, Noh Y, Dudhia J (2006) A new vertical diffusion package with an explicit treatment of entrainment processes. Mon. Wea. Rev: 134, 2318–2341.

Huffman GJ, Adler RF, Bolvin DT, Gu G, Nelkin EJ, Bowman KP, Hong Y, Stocker EF, Wolff DB (2007) The TRMM multisatellite precipitation analysis (TMPA): quasi-global, multiyear, combined-sensor precipitation estimates at fine scales. J Hydrometeorol: 8, 38–55. https://doi.org/10.1175/JHM560.1

Jones P., Lister DH, Osborn TJ, Harpham C, Salmon M, Morice CP (2012) Hemispheric and large-scale land surface air temperature variations: An extensive revision and an update to 2010, J. Geophys. Res: 117, D05127, https://doi:10.1029/2011JD017139

Kain, JS (2004) The Kain–Fritsch convective parameterization: An update. J. Appl. Meteor: 43, 170–181.

Kanamitsu M, Ebisuzaki W, Woollen J, Yang SK, Hnilo JJ, Fiorino M, Potter GL (2002) NCEP–DOE AMIP-II Reanalysis (R2). Bull. Amer. Meteor. Soc: 83, 1631–1643.

Kobayashi S, Ota Y, Harada Y, Ebita A, Moriya M, Onoda H, Onogi K, Kamahori H, Kobayashi C, Endo H, Miyaoka K, Takahashi K (2015) The JRA-55 Reanalysis: General specifications and basic characteristics. J. Meteorol. Soc. Jap. 93: 5-48. doi:10.2151/jmsj.2015-001.

Kumar KR, Attada R, Dasari HP, Vellore RK, Langodan S, Abualnaja YO, Hoteit I (2018) Aerosol optical depth variability over the Arabian Peninsula as inferred from satellite measurements. Atmospheric Environment 187: 346–357. https://doi.org/10.1016/j.atmosenv.2018.06.011

Kumar KR, Attada R, Dasari HP, Vellore RK, Abualnaja YO, Ashok K, Hoteit I (2019) On the Recent Amplification of Dust Over the Arabian Peninsula During 2002–2012. J. Geophys. Res. Atmos., 124, 23, 13220-13229.

Lenssen N, Schmidt G, Hansen J, Menne M, Persin A, Ruedy R, Zyss D (2019) Improvements in the GISTEMP uncertainty model. J. Geophys. Res. Atmosphere: 124, 6307-6326. doi:10.1029/2018JD029522

Lelieveld J, Proestos Y, Hadjinicolaou P, Tanarhte M, Tyrlis E, Zittis G (2016). Strongly increasing heat extremes in the Middle East and North Africa (MENA) in the 21st century. Climatic Change: 137, 245-260.

Mlawer EJ, Taubman SJ, Brown PD, Iacono MJ, Clough South America (1997) Radiative transfer for inhomogeneous atmosphere: RRTM, a validated correlated-k model for the longwave. J. Geophys. Res., 102: 16 663–16 682.

Nazrul Islam N, Almazroui M, Dambul R, Jones PD, Alamoudi AO (2015) Long-term change in seasonal temperature extremes over Saudi Arabia during 1981-2010. International J. Climatology: 35, 1579-1592.

Pal JS, Eltahir EA (2016) Future temperature in southwest Asia projected to exceed a threshold for human adaptability. Nature Climate Change: 6(2), 197.

Patricola CM, Cook KH (2007) Dynamics of the West African Monsoon under mid-Holocene precessional forcing: Regional climate model simulations. J Climate 20: 694-716. https://doi.org/10.1175/JCLI4013.1

Ravi Kumar K, Attada R, Dasari HP, Vellore RK, Abualnaja YO, Ashok K, Hoteit I (2019) On the recent amplification of dust over the Arabian peninsula during 2002–2012. J. Geophysical Research – Atmospheres: 124, 13,220–13,229. https://doi.org/10.1029/2019JD03069

Rohde R, Muller RA, Jacobsen R, Muller E, Perlmutter S, Rosewnfeld A, Wurtele J, Groom D, Wickham C. (2013) A new estimate of the average earth surface land temperature spanning 1753 to 2011. Geoinfor Geostat: An Overview 1:1. http://dx.doi.org/10.4172/2327-4581.1000101

Skamarock, W. C., J. B. Klemp, J. Dudhia, D. O. Gill, D. M Barker, W. Wang, and J. G. Powers, 2005:Adescription of theAdvanced Research WRF version 2. NCAR/TN-4081STR, 88 pp. [Available from NCAR Information Services, P.O. Box 3000, Boulder, CO 80307.]

Sorooshian S, Hsu KL, Gao X, Gupta HV, Imam B, Braithwaite D (2000) Evaluation of PERSIANN system satellite-based estimates of tropical rainfall. Bull Amer Meteorol Soc: 81, 2035-2046. https://10.1175/1520-0477(2000)081<2035:EOPSSE>2.3.CO;2

Vizy EK, Cook KH (2003) Connections between the summer East African and Indian rainfall regimes. J. Geophys. Res: 108, D16, 4510. https://doi.org/10.1029/2003JD003452

Vizy EK, Cook KH (2005) Evaluation of Last Glacial Maximum sea surface temperature reconstructions through their influence on South American climate. J. Geophys. Res: 110, D11105. https://doi.org/10.1029/2004JD005415

Vizy EK, Cook KH (2007) Relationship between Amazon and High Andes Rainfall. J. Geophys. Res . – Atmosphere: 112, D7107. https://doi.org/10.1029/2006JD0079980

Vizy EK, Cook KH (2017) Seasonality of the observed amplified Sahara warming trend and implications for Sahel rainfall. J Climate 30: 3073-3094. https://doi.org/10.1175/JCLI-D-16-0687.1

Vizy EK, Cook KH, Crétat J, Neupane N (2013) Projections of a wetter Sahel in the 21st century from global and regional models. J Climate 26: 4664-4687. https://doi.org/10.1175/JCLI-D-12-00533.1

Yang, CX, Giese BS, Wu LX (2014) Ocean dynamics and tropical Pacific climate change in ocean reanalyses and coupled climate models. J. Geophys. Res. – Oceans: 119, 7066-7077.

World Meteorological Organization (2009) Guidelines on Analysis of extremes in a changing climate in support of informed decisions for adaptation. Climate Data and Monitoring WCDMP-No. 72, WMO, Geneva.

Zhang X, Aguilar E, Sensoy S, Melkonyan H, Tagiyeva U, and co-authors (2005) Trends in Middle East climate extreme indices from 1950 to 2003. J. Geophys. Res. Atmos. 110: D22104, https://doi: 10.1029/2005JD006181

Zhu J, Wang S, Huang G (2019) Assessing Climate Change Impacts on Human-Perceived Temperature Extremes and Underlying Uncertainties. Journal of Geophysical Research: Atmospheres: 124, 3800-3821.

Table 1. Linear trends (K/decade) in annual-mean surface temperatures for 1979–2018. Statistically significant values at the 90%, 95%, and 98% confidence interval are italicized, boldfaced, and italicized and boldfaced, respectively, after taking autocorrelation into account using the method of Zwiers and von Storch (1995).

	Linear trends (K/decade)				amplification factor with respect to	
	Arabian Penin.	Tropics	Tropical Land	Global	Tropical Land	Global
CRU	**0.28**	---	**0.21**	---	1.4	---
GHCN	0.58	---	0.30	---	1.9	---
Berkeley	*0.41*	---	***0.22***	---	1.9	---
GISS	*0.41*	**0.14**	**0.23**	0.17	1.9	2.4
ERAI	**0.32**	***0.10***	***0.16***	*0.14*	2.0	2.3
JRA-55	*0.44*	**0.08**	***0.21***	*0.14*	2.1	3.1
MERRA2	**0.29**	*0.16*	**0.21**	*0.13*	1.4	2.3
Average	0.39	0.12	0.22	0.15	1.8	2.5

Table 2. Linear trends (K/decade) in surface temperature for 1979–2018 for December-January-February (DJF), March-April-May (MAM), June-July-August (JJA) and September-October-November (SON) averages. Statistically significant values at the 90%, 95%, and 98% confidence levels are italicized, boldfaced, and both italicized and boldfaced, respectively, after taking autocorrelation into account using the method of Zwiers and von Storch (1995).

Dataset	DJF				MAM			
	Arabian Penin.	Tropics	Tropical Land	Global	Arabian Penin.	Tropics	Tropical Land	Global
CRU	***0.29***		***0.22***		***0.30***		***0.19***	
GHCN	***0.47***		***0.30***		**0.65**		***0.29***	
Berkeley	**0.33**		***0.23***		***0.45***		***0.20***	
GISS	***0.37***	***0.14***	***0.24***	**0.15**	**0.48**	***0.14***	***0.23***	***0.17***
ERAI	*0.34*	***0.09***	***0.14***	**0.11**	***0.33***	***0.10***	***0.14***	***0.14***
JRA-55	**0.37**	***0.08***	***0.20***	***0.13***	***0.53***	***0.08***	***0.20***	***0.14***
MERRA2	*0.25*	***0.16***	***0.21***	**0.12**	***0.35***	***0.15***	***0.18***	***0.12***
Average	0.35	0.12	0.22	0.13	0.44	0.12	0.20	0.14

Dataset	JJA				SON			
	Arabian Penin.	Tropics	Tropical Land	Global	Arabian Penin.	Tropics	Tropical Land	Global
CRU	***0.24***		***0.20***		***0.34***		**0.23**	
GHCN	0.68		**0.30**		0.60		0.34	
Berkeley	*0.50*		***0.22***		**0.43**		***0.25***	
GISS	*0.47*	**0.15**	***0.23***	**0.16**	***0.36***	***0.15***	**0.25**	0.20
ERAI	**0.35**	***0.12***	***0.17***	***0.14***	***0.33***	***0.11***	***0.21***	0.17
JRA-55	0.50	***0.09***	***0.22***	***0.13***	**0.43**	**0.09**	***0.25***	*0.17*
MERRA2	**0.30**	**0.18**	***0.22***	**0.12**	**0.30**	**0.18**	***0.25***	0.16
Average	0.43	0.13	0.22	0.14	0.40	0.13	0.25	0.18

Table 3. Trends (W/m^2-40 yr) and standard deviations (in parentheses) of the annual-mean surface heat balance components averaged over the tropics (30°S–30°N) and the Arabian Peninsula (15°N–25°N, 40°E–55°E) in the ERAI, JRA55, and MERRA2 reanalyses. Statistically significant values are calculated accounting for autocorrelation using the method of Zwiers and von Storch (1995). Levels at the 90%, 95%, and 98% confidence interval are italicized, boldfaced, and both italicized and boldfaced, respectively.

	Tropical ERAI	Tropical JRA55	Tropical MERRA2	Arabian ERAI	Arabian JRA55	Arabian MERRA2
Solar absorbed (S_{ABS})	-1.70 (1.27)	-2.83 (1.16)	-5.81 (1.92)	-0.83 (1.56)	-0.89 (1.22)	-1.42 (2.06)
Longwave back (F_{BACK})	**2.75** (1.45)	***3.51*** (1.46)	*5.25* (1.89)	**8.51** (3.76)	**9.90** (3.92)	6.11 (3.37)
Upward longwave (F_{UP})	***2.54*** (1.08)	**2.80** (1.12)	*3.80* (1.42)	**8.06** (3.42)	*10.86* (4.30)	*6.94* (3.04)
Net upward longwave (F_{UP}-F_{BACK})	-0.21 (0.57)	-0.71 (0.52)	*-1.46* (0.56)	-0.45 (2.49)	0.96 (2.97)	0.83 (2.36)
Net radiative Heating (S_{ABS}+F_{BACK}-F_{UP})	-1.49 (0.88)	-2.11 (0.78)	-4.35 (1.58)	-0.38 (1.05)	-1.85 (1.95)	*-2.25* (1.22)
Sensible heat flux (H_S)	0.33 (0.27)	-0.50 (0.27)	0.42 (0.39)	*1.63* (1.05)	***1.76*** (1.03)	0.98 (1.31)
Latent heat flux (H_L)	9.10 (2.91)	5.87 (2.20)	6.52 (2.71)	-0.35 (1.70)	-3.50 (2.65)	*-3.08* (1.69)
Redistribution of heat (D)	-10.92 (3.63)	-7.48 (2.63)	-11.29 (4.07)	***-1.66*** (0.59)	-0.11 (0.27)	-0.15 (0.18)

Table 4. Surface temperature differences (K) and trends [K/decade] over the Arabian Peninsula averaging region (15°N–25°N, 40°E–55°E) for the M21 and L21 simulations. All differences are statistically significant at the 98% confidence interval (italicized and boldfaced).

Month	Difference M21-CTL (K)	Warming Rate M21-CTL (K/decade)	Difference L21-CTL (K)	Warming Rate L21-CTL (K/decade)
DJF	***2.5***	0.48	***4.3***	0.42
MAM	***2.4***	0.46	***4.6***	0.45
JJA	***2.8***	0.54	***5.6***	0.55
SON	***3.0***	0.58	***5.7***	0.56
Annual	***2.7***	0.52	***5.1***	0.50

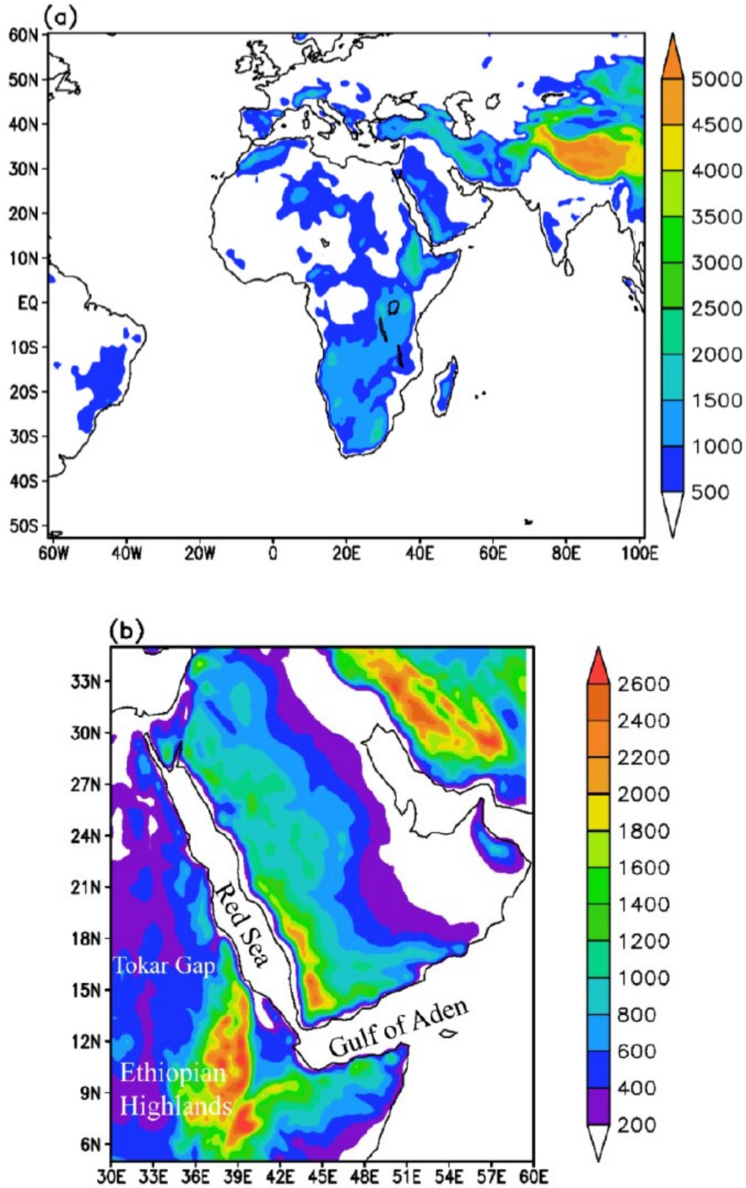

Figure 1. (a) Outer domain of the climate model simulation with topography as resolved at 90 km grid spacing. (b) Inner domain of the simulation with topography as resolved at 30 km grid spacing.

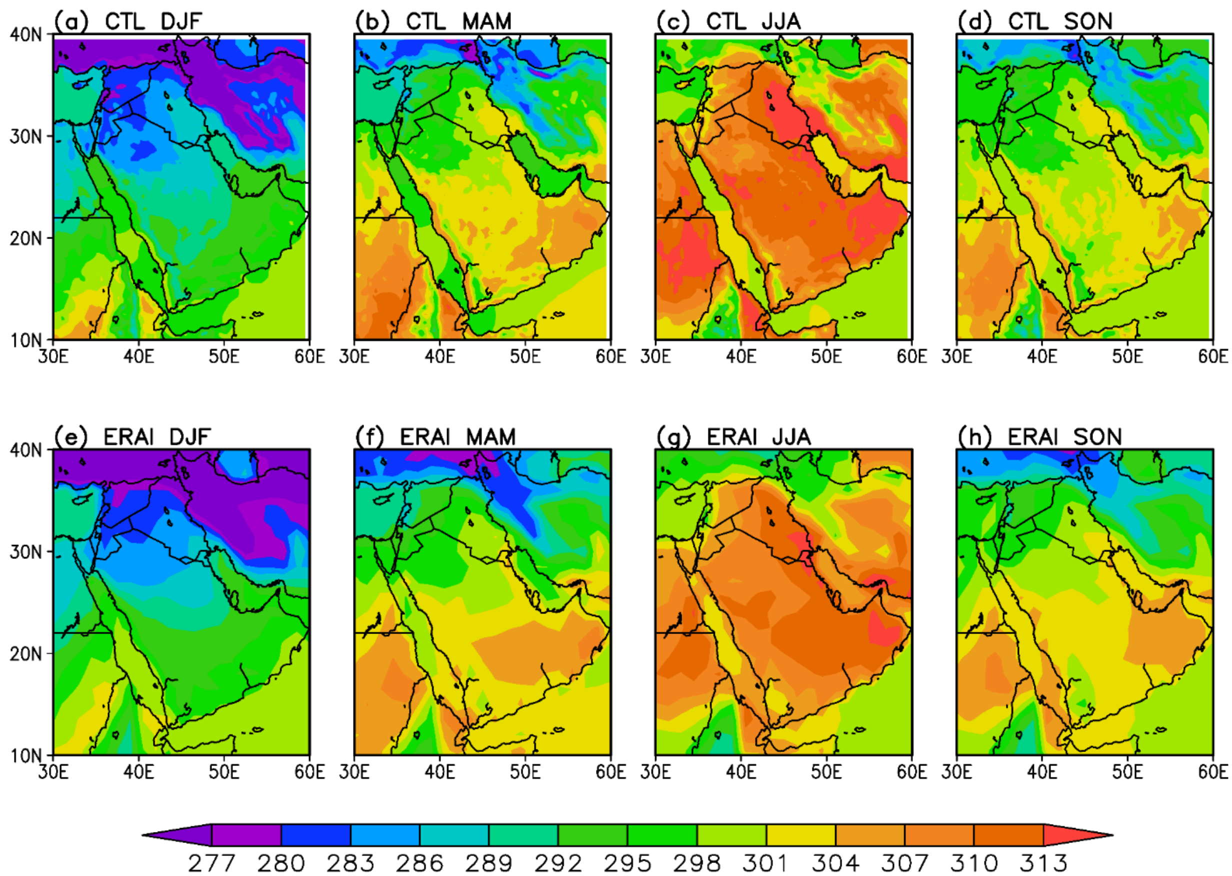

Figure 2. Surface temperature (K) for the ensemble-mean CTL simulation for (a) DJF, (b) MAM, (c) JJA, and (d) SON. Additionally, surface temperature (K) for the 1989-2008 mean from the ERAI reanalysis for (e) DJF, (f) MAM, (g) JJA, and (h) SON. Values from the JRA-55 reanalysis (not shown) are similar to the ERAI values.

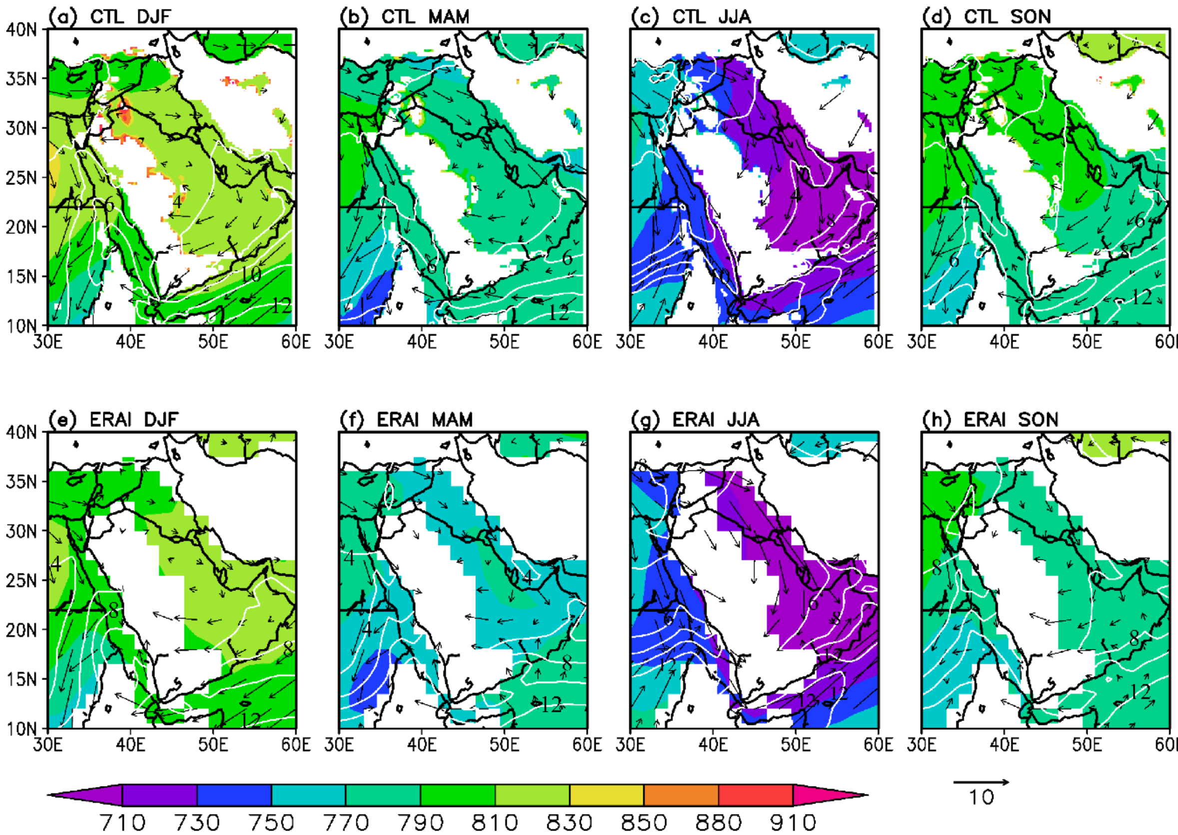

Figure 3. 925-hPa geopotential heights (shaded; contour interval 20 gpm), specific humidity (contours; contour interval 10^{-3} kg-H_2O/kg-air), and winds (vectors, scale at bottom right in ms-1) from the CTL simulation ensemble mean for (a) DJF, (b),MAM, (c) JJA, and (d) SON. 925-hPa geopotential heights (shaded; contour interval 20 gpm), specific humidity (contours; contour interval 10^{-3} kg-H_2O/kg-air), and winds (vectors, scale at bottom right in ms-1) from the ERAI climatology for (e) DJF, (f),MAM, (g) JJA, and (h) SON. For the simulation, every 10^{th} vector is plotted and for the ERAI reanalysis every other vector is plotted. White regions indicate where topography extends above the 925-hPa level.

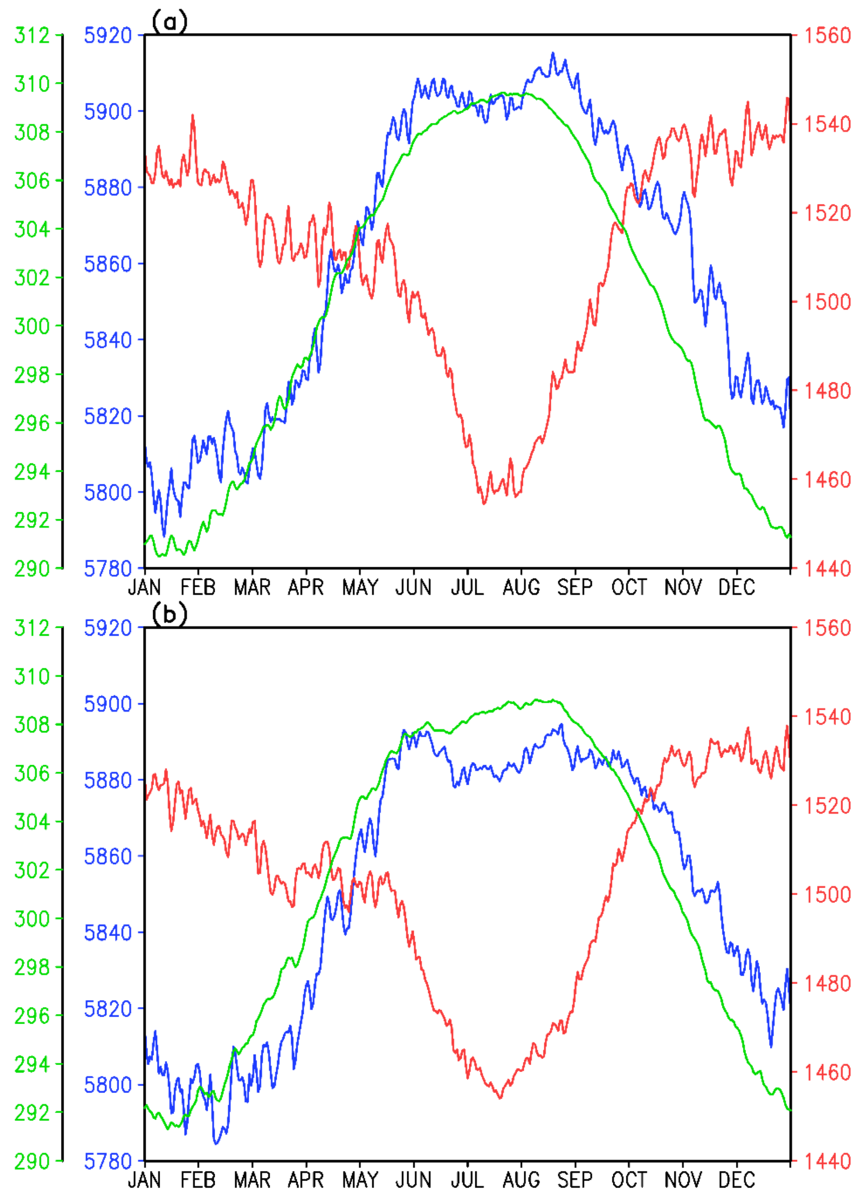

Figure 4. Seasonal variations of daily 500-hPa geopotential heights (blue lines; inner left axis labels), 850-hPa geopotential heights (red lines; right axis label), and surface temperatures (green lines; outer left axis labels) averaged over the Arabian Peninsula (15ºN – 30ºN; 35ºE to 55ºE) from the (a) CTL simulation and (b) ERAI reanalysis averaged from 1981-2000. Shading indicates June, July, and August.

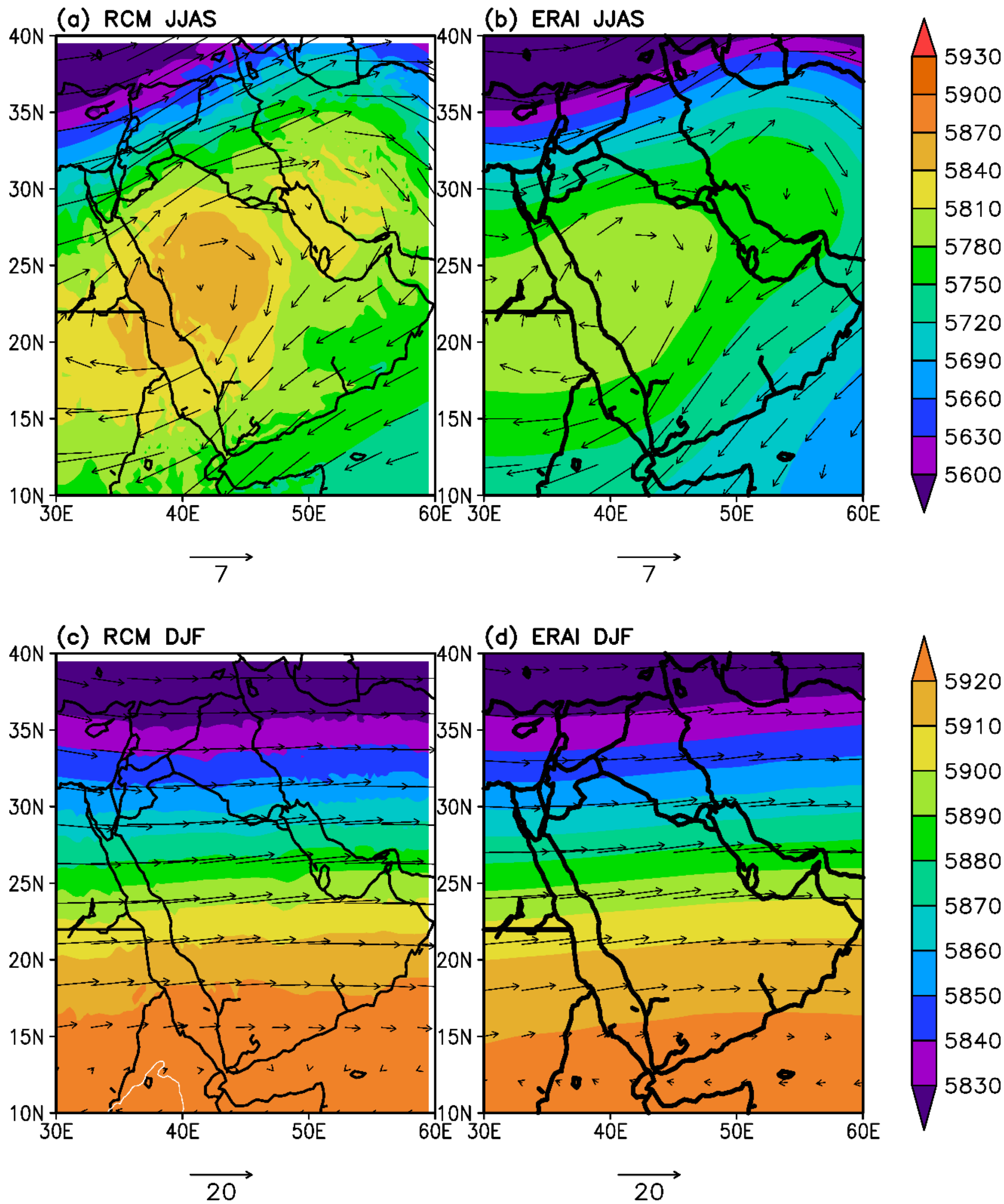

Figure 5 Geopotential heights (gpm; shaded) and winds (m/s; vectors) at 500 hPa for the (a) CTL simulation in JJAS, (b) ERAI reanalysis in JJAS, (c) CTL simulation in DJF, and (d) ERAI reanalysis in DJF. Vector scales in m/s are below each panel.

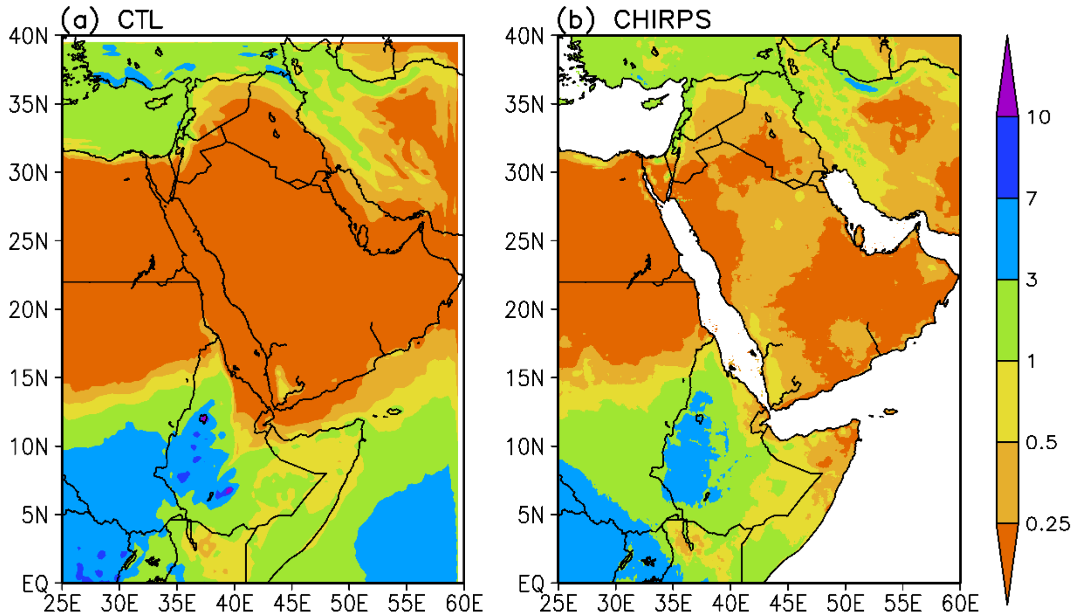

Figure 6. Annual mean precipitation (mm/day) over the Arabian Peninsula and vicinity for the (a) CTL simulation and the (b) CHIRPS2 precipitation dataset averaged from 1989-2008.

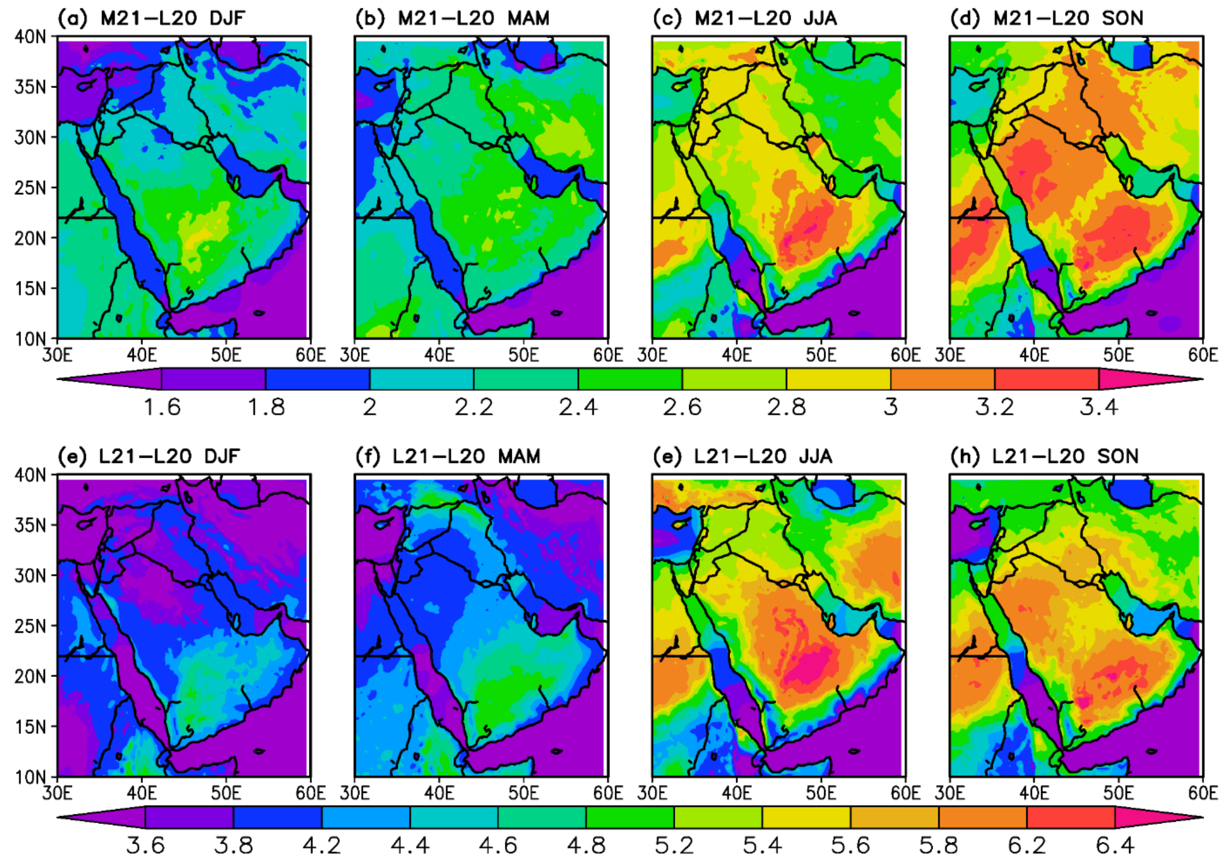

Figure 7. Simulated differences in surface temperature (K) between the MID21 and CTL simulations for (a) DJF, (b) MAM, (c) JJA, and (d) SON. Simulated differences in surface temperature (K) between the LATE21 and CTL simulations for (e) DJF, (f) MAM, (g) JJA, and (h) SON. Shading interval is 0.2 K.

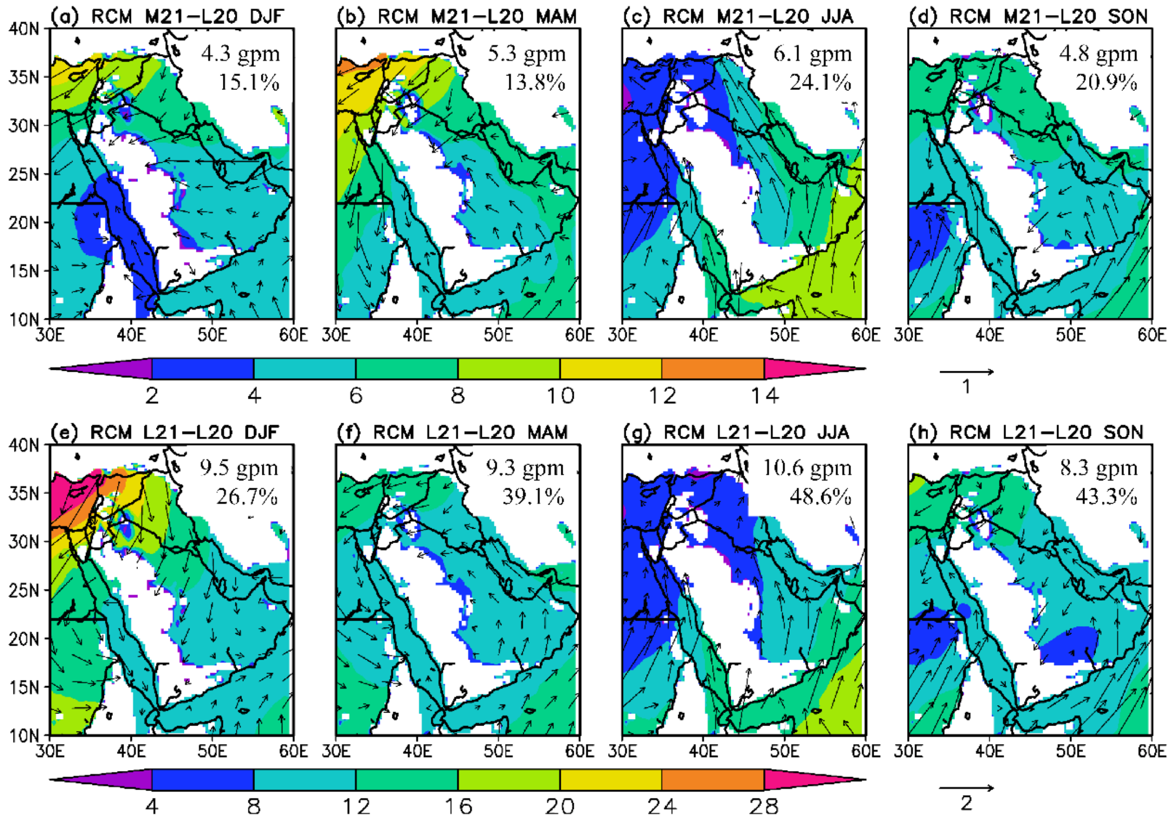

Figure 8. Simulated mid-21st c. differences in 850-hPa geopotential heights (shaded; contour interval 2 gpm) and winds (vectors, scale at bottom right in ms^{-1}) for (a) DJF, (b),MAM, (c) JJA, and (d) SON. Simulated late-21st c. differences in 850-hPa geopotential heights (shaded; contour interval 4 gpm) and winds (vectors, scale at bottom right in ms^{-1}) from the ERAI climatology for (e) DJF, (f),MAM, (g) JJA, and (h) SON. Every 10th vector is plotted. Numbers in the upper right corner of each panel indicate differences in geopotential heights (gpm) and specific humidity (% change) over the Arabian Peninsula averaging region (15-25N; 40-55E).

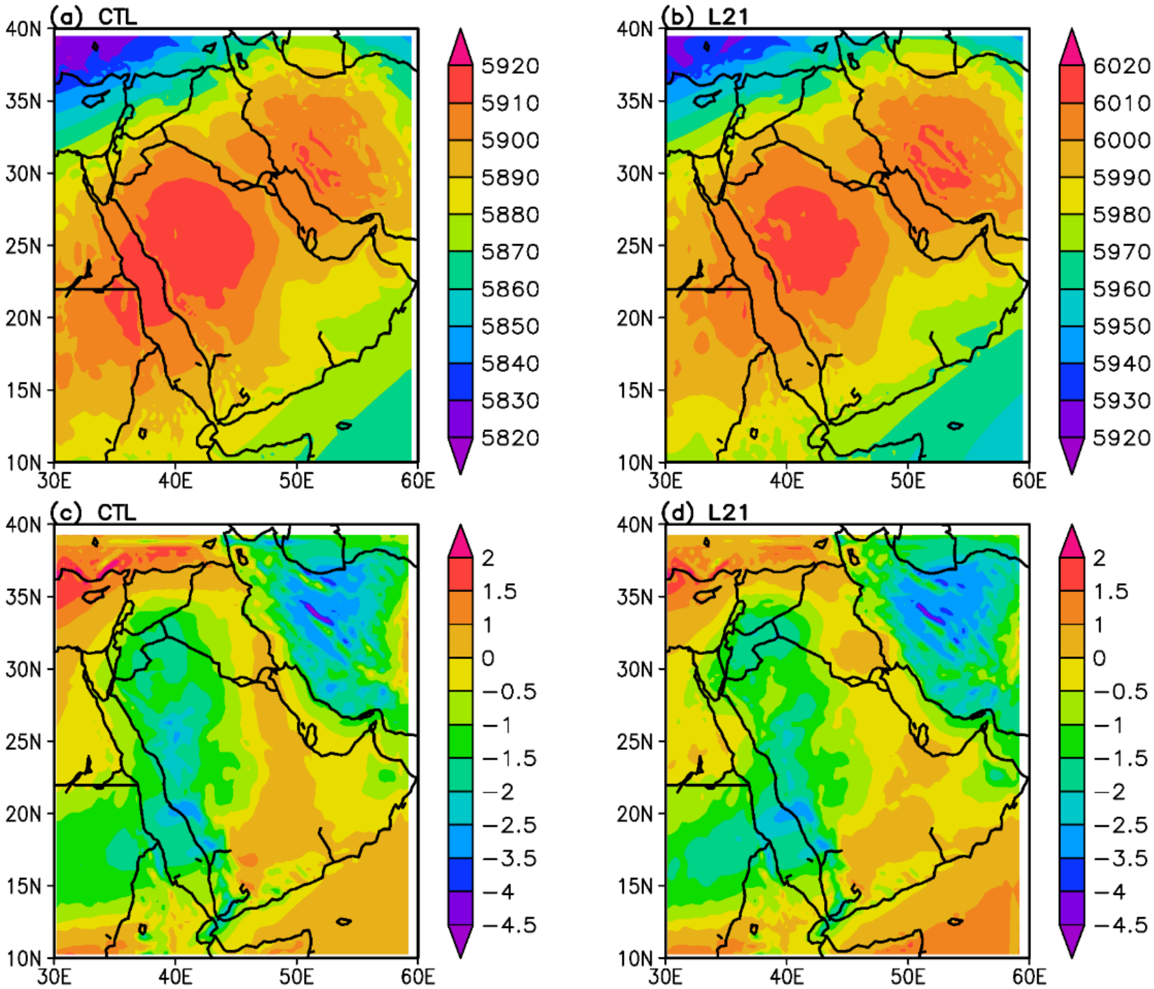

Figure 9. July 500-hPa geopotential heights (m) for the (a) CTL and (b) L21 ensemble means. Note differences in the shading levels indicated by the color bars. July 500-hPa relative vorticity (10^{-5} s^{-1}) for the (c) CTL and (d) L21 ensemble means, with the same shading levels.

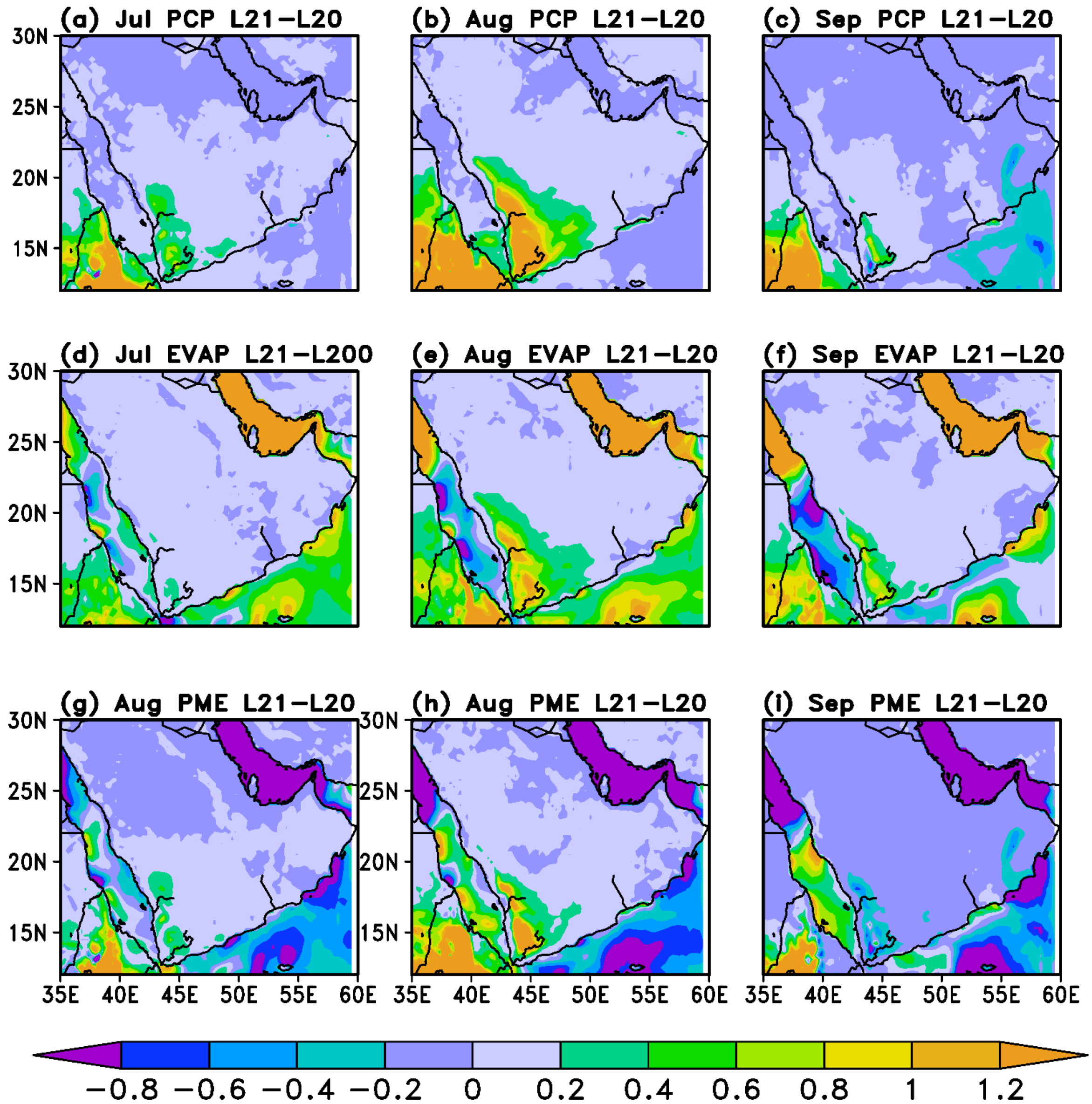

Figure 10. Differences in monthly mean precipitation (mm/day) between the L21 and CTL simulations for (a) July, (b), August, and (c) September. Differences in monthly mean evaporation (mm/day) between the L21 and CTL simulations for (d) July, (e), August, and (f) September. Differences in monthly mean "precipitation minus evaporation" (mm/day) between the L21 and CTL simulations for (g) July, (h), August, and (i) September.

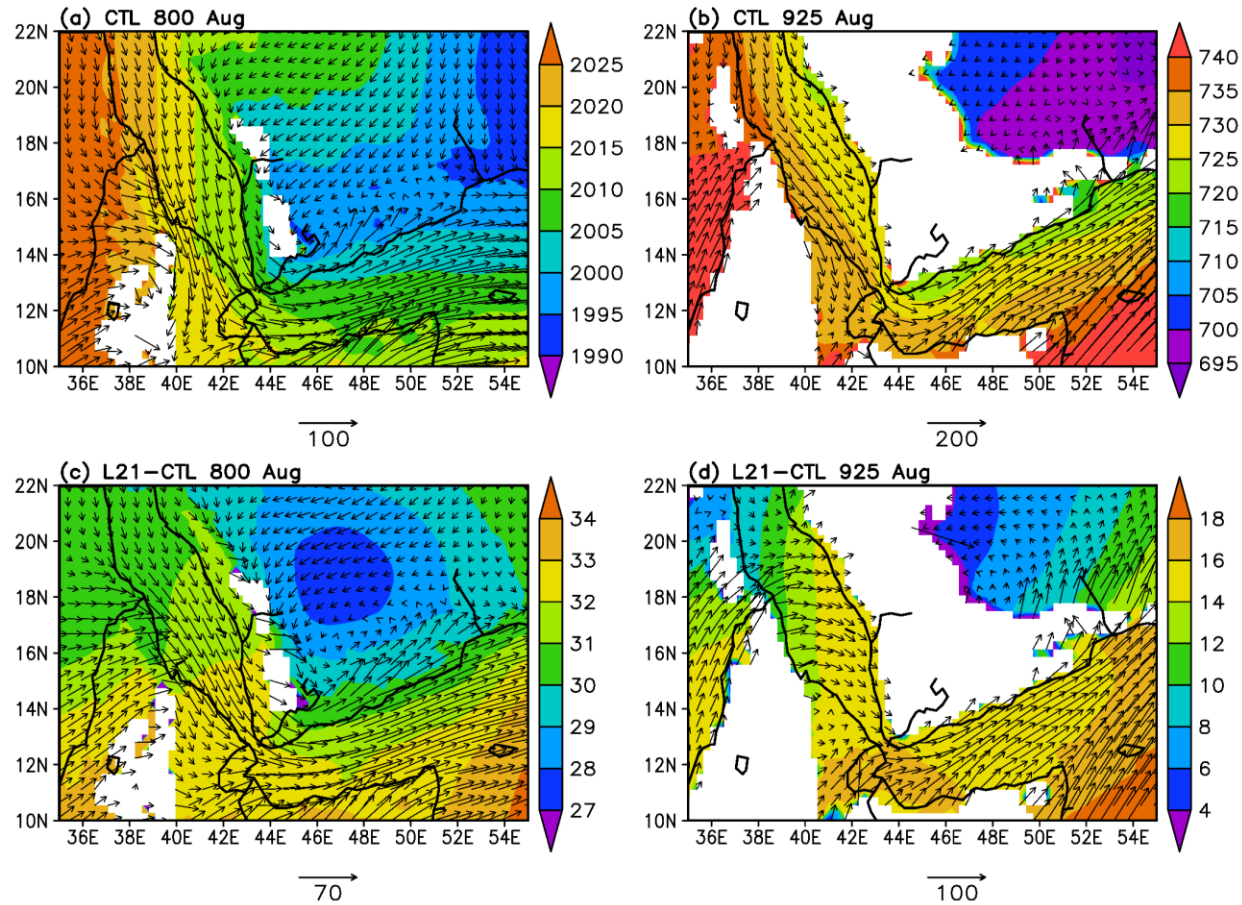

Figure 11. Geopotential heights (gpm; shading) and moisture transport vectors [10^3kg-H_2O/kg-air)(m/s)] in August from the CTL simulation at (a) 800 hPa and (b) 925 hPa. Differences in geopotential heights (gpm; shading) and moisture transport vectors [10^3kg-H_2O/kg-air)(m/s)] in August between the L21 and CTL simulations at (a) 800 hPa and (b) 925 hPa. White areas indicate regions where the topography extends above the pressure level.

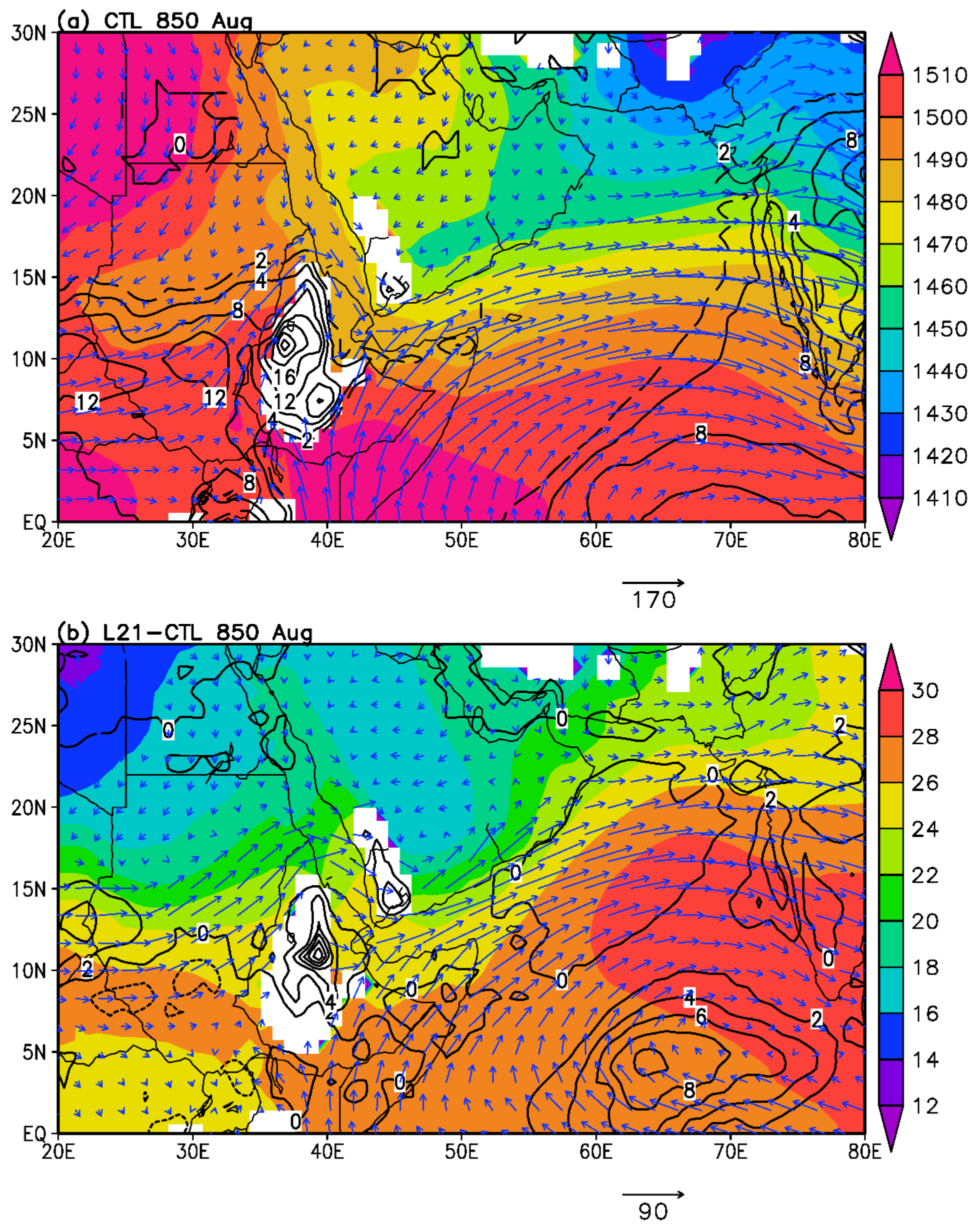

Figure 12. (a) August geopotential height (gpm; shaded) and moisture transport (units; vectors) at 850 hPa with precipitation (mm/day; contours) from the 90-km resolution (outer domain) CTL simulation ensemble mean. Precipitation contour interval is 4 mm/day, with the 2 mm/day contour dashed. (b) Differences in the August 850-hPa geopotential height (gpm; shaded), 850-hPa moisture transport (units; vectors), and precipitation (mm/day; contours) between the 90-km resolution L21 and CTL simulations. Precipitation contour interval is 2 mm/day.

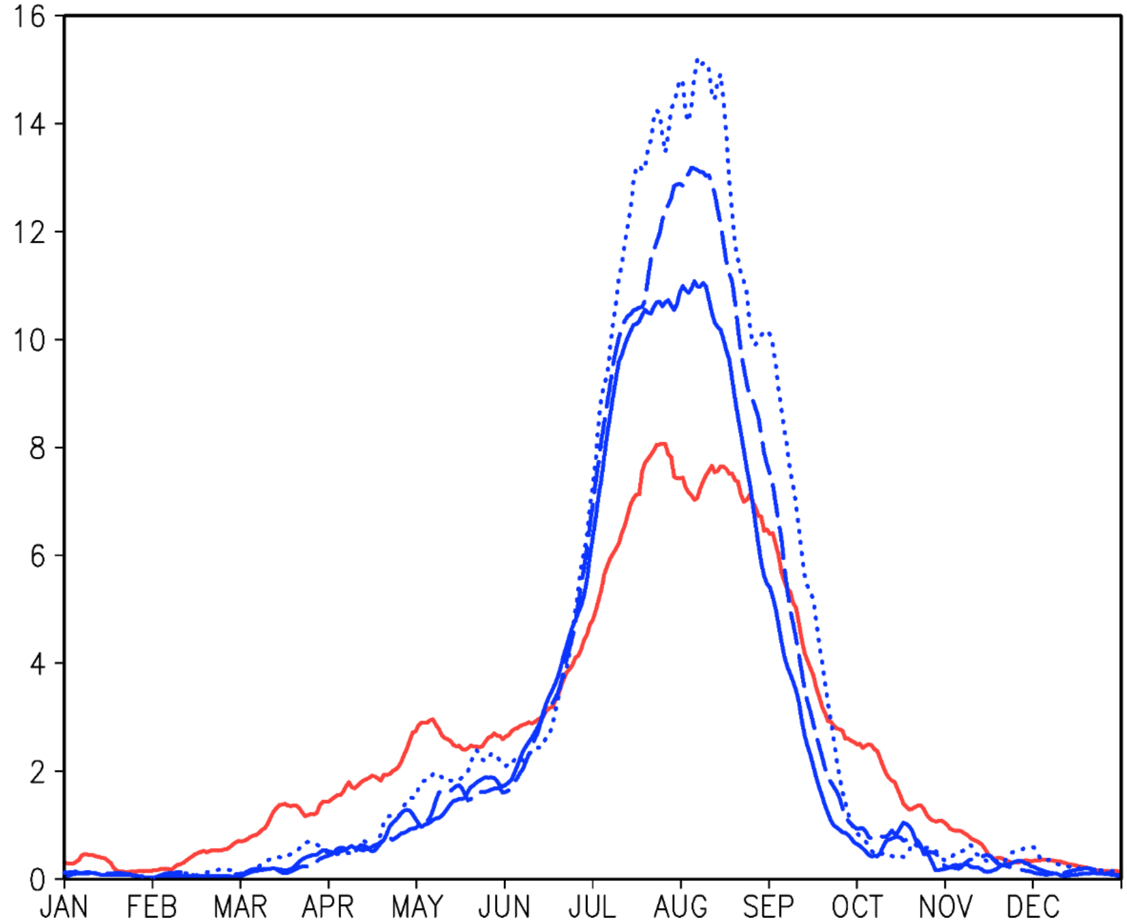

Figure 13. Climatological annual rainfall averaged over northern Ethiopia (36E-42E; 8N-15N) from the CHIRPS observations (red line) and the model simulations (blue) for the CTL (solid line), M21 (dashed line), and L21 (dotted line) ensemble-mean simulations.

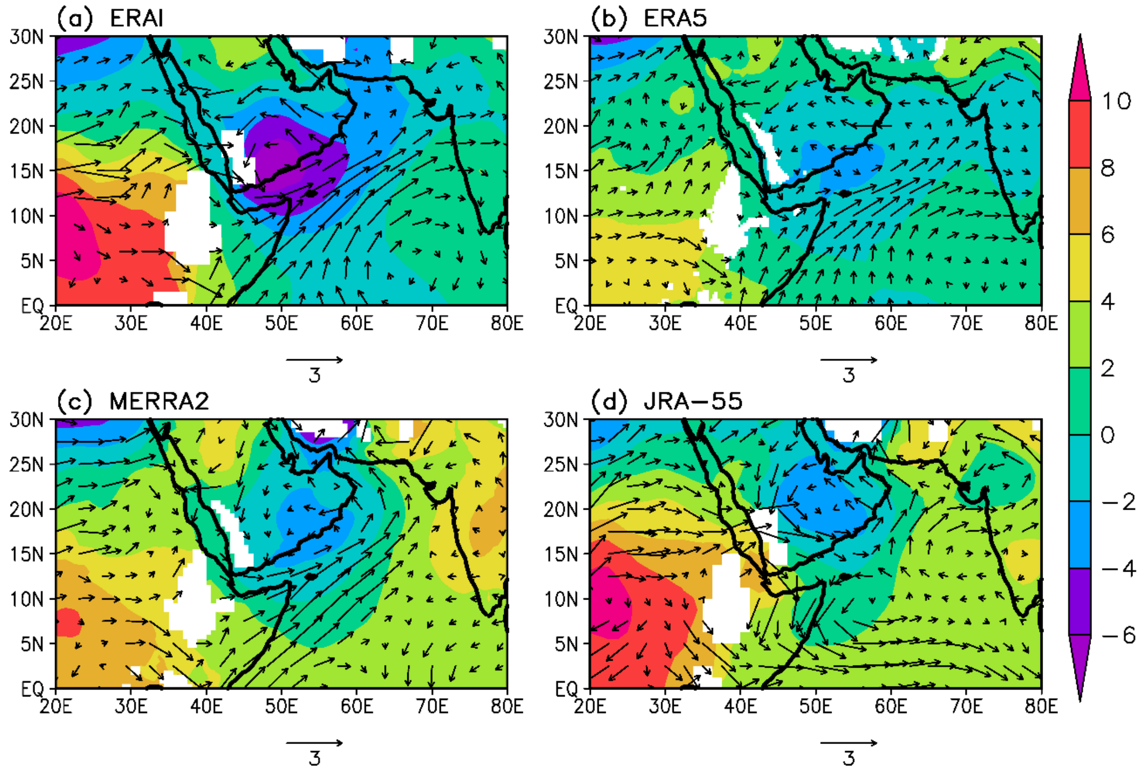

Figure 14. Decadal differences in June-July-August-September mean 850-hPa geopotential heights (shaded; gpm) and winds (vectors; scale in m/s) from the (a) ERAI, (b) ERA5, (c) MERRA2, and (d) JRA-55 reanalyses. The dashed blue contour in (a) marks regions where the topography rises above the 850-hPa pressure level. Differences between the 2010-2019 and the 1979-1988 averages are shown except for MERRA2, which is the difference between the 2010-2018 and 1980-1989 averages.